



Contents lists available at ScienceDirect



He-ion irradiation effects on the microstructure stability and size-dependent mechanical behavior of high entropy alloy/Cu nanotwinned nanolaminates

H.H. Chen¹, Y.F. Zhao¹, J.Y. Zhang^{*}, Y.Q. Wang, G.Y. Li, K. Wu, G. Liu^{**}, J. Sun

State Key Laboratory for Mechanical Behavior of Materials, Xi'an Jiaotong University, Xi'an, 710049, People's Republic of China



ARTICLE INFO

Keywords:

High-entropy alloys
Nanolaminated structure
Interfaces
Nanotwins

ABSTRACT

High entropy alloys (HEAs) have attracted extensive attention due to their excellent properties in harsh environments. In this work, we prepare HEA/Cu (HEA = FeCoCrNi) nanotwinned nanolaminates (NTNLs) with equal individual layer thickness (h) and study the He-ion irradiation effects on their deformation behavior and mechanical properties. With decreasing h the microstructure of HEA/Cu NTLNs transits from the nanolayered structure with nanotwins confined in the isolated layers at large $h \geq 25$ nm to the columnar grained single crystal-like structure with nanotwins penetrated across the coherent layer interface(s) at small $h < 25$ nm. Compared with the as-deposited HEA/Cu NTLNs showing notable detwinning behavior, in particular at small h , the nanotwins in irradiated samples are difficult to detwin owing to the He defects pinning effect on twin boundaries. It appears that both as-deposited and irradiated HEA/Cu NTLNs manifest the trend of "smaller is stronger". Unlike the reported monotonically increased/reduced irradiation hardening with h in conventional bimetal nanolaminates, a minimum irradiation hardening occurs in the present HEA/Cu NTLNs. Unexpectedly, the as-deposited HEA/Cu NTLNs manifest positive reduced strain rate sensitivity (SRS) m with decreasing h , while their irradiated siblings exhibit the transition from positive to negative SRS m . The size-dependent mechanical properties of HEA/Cu NTLNs are rationalized by the partial-based mechanism in combination with the stability of nanotwins.

1. Introduction

Designing damage tolerant structural materials is a grand challenge for their applications in advanced nuclear fission reactors and fusion facilities, often suffering from a high level of ion irradiation (Beyerlein et al., 2015; Zhang et al., 2018b). Irradiation-induced defects are created in the form of Frenkel pairs (*i.e.*, vacancies and interstitials), which then evolve into larger point defect clusters, such as bubbles, voids, and dislocation loops, thus degrades the mechanical performance of these materials, *e.g.* hardening, embrittlement and swelling (Zinkle and Was, 2013). To reduce irradiation damage, apart from limiting the production of defects by tuning materials' composition, the key is to enhance the recombination/annihilation rate of irradiation defects as soon as they are created via

* Corresponding author.

** Corresponding author.

E-mail addresses: jinyuzhang1002@mail.xjtu.edu.cn (J.Y. Zhang), lgsammer@mail.xjtu.edu.cn (G. Liu).

¹ These authors contribute equally to this paper.

increasing the density of defect sinks for interstitials and vacancies (Yang et al., 2017).

In fact, the alloying strategy is quite effective to limit the production of irradiation-induced point defects in materials, in particular for the concentrated solid-solution alloys, including high entropy alloys (HEAs), in which the compositional complexity and the lattice distortions can effectively alter the defect migration behavior (Fan et al., 2019c; Jawaharam et al., 2020; Lu et al., 2016, 2017a). It is unveiled that the tailored interstitial defect cluster motion in FCC HEAs, e.g. FeCoCrNi, from a long-range 1D mode to a short-range 3D mode renders a sharply increased vacancy–interstitial recombination rate (Lu et al., 2016), which ultimately enhances their irradiation tolerance. Meanwhile, the core effects of HEAs, including high-entropy effects, sluggish diffusion, severe lattice distortion and cocktail effects, enable these coarse-grained (CG) HEAs to possess excellent mechanical properties, such as superior strength (Fang et al., 2019; Ganji et al., 2017; George et al., 2019; Lu et al., 2017b; Wang et al., 2020; Wu et al., 2018b), high ductility (Ding et al., 2018; George et al., 2019; Hasana et al., 2019; He et al., 2014; Li et al., 2017a; Lu et al., 2017b; Zhang et al., 2020), great thermal stability (George et al., 2019; Jiang et al., 2017; Juan et al., 2015; MacDonald et al., 2019; Schuh et al., 2015; Zhao et al., 2018), excellent irradiation resistance (Fan et al., 2019c; Jawaharam et al., 2020; Lu et al., 2017a; Tsai et al., 2008) and good corrosion resistance (Gludovatz et al., 2014; Tang et al., 2015). For example, CG FeCoCrNiMn HEAs exhibit exceptional damage tolerance with tensile strength >1.0 GPa and fracture toughness >200 MPa m^{1/2} (Zhang et al., 2015c). In this sense, the HEAs that break traditional principle for alloy design open a new area for exploring new damage tolerant materials serving in harsh environments (Cantor et al., 2004; Yeh et al., 2004; Zhang et al., 2014b).

Previous studies have demonstrated that the irradiation tolerance of a material can be enhanced through introducing defect sinks, such as grain boundaries (GBs) (Chen et al., 2013; Han et al., 2013; Jawaharam et al., 2020) and twin boundaries (TBs) (Fan et al., 2019a; Li et al., 2011, 2015; Yu et al., 2013a), both of which facilitate the recombination of irradiation-induced defects and defect clusters. Refining grain sizes of HEAs into the nanocrystalline (NC) regime to drastically increase the volume density of GBs is thus a popular way for reducing residual defects in irradiated materials (Jawaharam et al., 2020). Indeed, these NC metals manifest superior irradiation tolerance to their CG counterparts (Han et al., 2013), but they inevitably experience irradiation-enhanced GB motion and growth (Kaoumi et al., 2008) accompanied with degradation of mechanical properties. Coherent TBs (CTBs) are in general a special type of GBs without apparent free volume and are normally considered to be ineffective defect sinks (Beyerlein et al., 2015; Zhang et al., 2018b). However, the CTBs can remove irradiation-induced defects, such as stacking-fault (SF) tetrahedras in FCC metals (e.g. Ag), and interstitial clusters (Yu et al., 2013a). A recent study (Li et al., 2015) has also shown that the interactions of CTBs with defects induce steps and SFs. These steps provide fast-diffusion channels to promote point defect migration and annihilation mainly due to the confined migration from 3D to 1D along dislocations. Therefore, introducing a high-density of CTBs, in particular these nanotwins with extremely small thickness (λ), into NC HEAs would further enhance their irradiation tolerance. To the best of authors' knowledge, however, there is no study about the irradiation behavior of nanotwinned (NT) HEAs, e.g. the FCC FeCoCrNi system, in the nanoscale.

Apart from the approaches mentioned above, the irradiation tolerance of HEAs can be dramatically enhanced by introducing a high density of heterophase interfaces into their microstructure to synthesize the nanolaminates (NLs) with layer thickness (h) less than 100 nm (Zhang et al., 2019). The basic strategy exploits the idea that interfaces as efficient defect sinks are favorable regions, where the vacancy–interstitial combination rates can be strongly increased relative to the adjacent bulk crystals (Beyerlein et al., 2015; Zhang et al., 2018b). Tremendous studies have been dedicated to the irradiation behavior of conventional bimetal NLs, such as FCC/BCC Cu/Nb (Hansen et al., 2013), Cu/Mo (Zhang et al., 2016) and Cu/V (Fu et al., 2010), FCC/FCC Cu/Co (Chen et al., 2015), Cu/Ag (Wang et al., 2018) and Ni/Ag (Yu et al., 2013b), FCC/HCP Cu/Zr (Liang et al., 2019), BCC/BCC Fe/W (Li et al., 2009), and BCC/HCP Zr/Mo (Wu et al., 2018a) and Zr/Nb (Frutos et al., 2015). It is uncovered that a high volume fraction of interfaces gives rise to high strength, great strain rate sensitivity (SRS, m) and superior irradiation tolerance (Zhang et al., 2016), and that the incoherent interfaces exhibit much better irradiation tolerance than its coherent component (Beyerlein et al., 2015; Zhang et al., 2018b). Moreover, the nanotwins, serving as dislocation barriers and/or sources on the one hand, can enhance the mechanical properties of NLs (Anderoglu et al., 2010; Cao et al., 2018; Feng et al., 2017; Liu et al., 2011; Lu et al., 2009; Niu et al., 2012; Zheng et al., 2013), and they, acting as defect sinks on the other hand, can enhance their irradiation tolerance (Fan et al., 2019a; Li et al., 2012, 2015; Yu et al., 2013a). Thus, the nanotwinned (NT) NLs (NTNLs) containing a HEA constituent, e.g. HEA/Cu NTNLs would be expected to display great irradiation tolerance and superior mechanical properties via the combination of planar defects, i.e., GBs, TBs and interfaces. Specifically, the defect dynamics of interstitial clusters between FeCoCrNi and Cu are markedly different, i.e., short-range 3D motion in the former vs long-range 1D motion in the latter (Lu et al., 2016; Yang et al., 2017), meaning the mobility of defects in Cu is higher. As such, the contribution of a HEA phase on radiation resistance of FCC/FCC HEA/Cu interface is significant. Owing to the unique microstructure of HEAs, the HEA/Cu interfaces are expected to be more effective to absorb the irradiation defects and inhibit the point defects inter-diffusion at interfaces, compared with conventional FCC/FCC bimetal NLs (e.g. Cu/Ag and Ag/Ni).

For these un-irradiated bimetal NLs, their strengthening mechanisms change from the dislocations pile-up to the confined layer slip (CLS) and to the dislocation cutting across the interface with decreasing h (Cao et al., 2017, 2019; Misra et al., 2005; Zhang et al., 2015b). For the (He) ion irradiated bimetal NLs, their size-dependent strengthening behavior is often captured by the dispersed barrier hardening model, in which the irradiation-induced defects (e.g. He bubbles) are assumed to act as barriers to gliding dislocations in the slip plane based on Orowan hardening (Beyerlein et al., 2015; Zhang et al., 2018b). It should be emphasized that, similar to the cases of NC pure metals (Lu et al., 2009; Ritchie, 2011), as the grain size (d) is reduced into submicron- and nano-scales, these HEAs often exhibit increased strength but greatly reduced tensile ductility (Fu et al., 2016; Schuh et al., 2015) or deformability (Fan et al., 2019b). In this case, the NL strategy can be also utilized to suppress the nucleation/propagation of microcracks and enhance trans-grain slip resistance, thus achieving great plasticity for NC HEAs without sacrificing their high strength (Beyerlein and Wang, 2019; Liang et al., 2020; Misra et al., 1998; Niu et al., 2012; Yan et al., 2013). Moreover, the laminated structure represents an ideal vehicle for the exploration of length scale-dependent plasticity of HEAs (under the constraining condition). However, how such kind of NTNLs as well

as the NT HEA constituent would respond under mechanical loading before and after ion-irradiation remains largely unexplored.

Motivated by above issues, here we first introduce the NT HEA (HEA = FeCoCrNi) into the nanolaminated structure, since these HEAs bear several desirable intrinsic properties as mentioned above. We investigate the microstructure evolution and size-dependent mechanical properties of HEA/Cu NTNLs before and after He ion-irradiation to uncover their underlying deformation mechanisms. It is found that both un-irradiated and irradiated HEA/Cu NTNLs manifest the trend of “smaller is stronger”. Unlike the reported monotonically increased or reduced irradiation hardening with h in conventional bimetal NLS, a minimum irradiation hardening occurs in HEA/Cu NTNLs. Compared with the un-irradiated HEA/Cu NTNLs with positive SRS m , the irradiated samples exhibit the transition from positive to negative SRS m with decreasing h . Specifically, the He-implantation can be utilized to stabilize the microstructure, e.g. nanotwins, of HEA/Cu NTNLs under plastic deformation.

2. Experimental procedures

2.1. Materials preparation and He implantation

The HEA/Cu (HEA = FeCoCrNi) NTNLs with equal individual layer thickness (h) in the range of 5–150 nm were deposited on HF-etched (111)-Si wafers by direct current (DC) magnetron sputtering at room temperature. Pure Cu (99.995%) and HEA (99.95%) targets were used to prepare HEA/Cu NTNLs with the total thickness of ~1.5 μm . The sputtering chamber was evacuated to a base pressure of 4×10^{-4} Pa before deposition. The deposition rates for Cu and HEA are ~0.12 and ~0.125 nm s^{-1} , respectively. The substrate was neither heated nor cooled during the deposition process. The first layer on the substrate is Cu and the cap layer is HEA. The implantation was performed at room temperature with a He ion energy of 40 keV and a total fluence of 1×10^{17} ions· cm^{-2} . All the irradiation experiments were performed using BNU-400 ion implanter and the base pressure was maintained at 1×10^{-4} Pa. He concentration vs penetration depth was simulated by SRIM software.

2.2. Microstructure characterization

X-ray diffraction (XRD) experiments were carried out using a Bruker D8 Discover powder X-ray diffractometer with Cu K α radiation at room temperature to determine the phase structure and crystallographic orientations of the as-deposited and irradiated HEA/Cu NTNLs. Transmission electron microscopy (TEM) was performed on JEOL JEM-2100F electron microscope equipped with energy dispersive spectroscopy (EDS) at the 200 kV accelerating voltage, to characterize the internal features of HEA/Cu NTNLs. To investigate the microstructural evolution during plastic deformation, post-mortem TEM observations were also performed on the indented HEA/Cu NTNLs. The TEM foils were prepared using a FEI Helios NanoLab 600i dual-beam focus ion beam (FIB) system via the lift-out technique.

2.3. Nanoindentation tests

Nanoindentation hardness (H) tests were conducted on all film materials using a TI950 TriboIndenter (Hysitron, Minneapolis, MN) equipped with a standard Berkovich diamond indenter with a nominal tip radius of curvature of 50 nm under the load-controlled mode at room temperature. The loading time varied from 5 to 100 s, correspondingly the loading strain rates spanning from 0.005 to 0.1 s^{-1} , in order to obtain the SRS index m . The SRS m is experimentally defined as the slope of the double logarithmic plot of hardness H and $\dot{\epsilon}$ under isothermal conditions, which can be expressed as $m = \frac{d \log(H)}{d \log(\dot{\epsilon})}$. The allowed drift rate was set as 0.01 nm s^{-1} , which is 10 times smaller than the typical value (0.1 nm s^{-1}) to guarantee the reliability and accuracy of the measurements. A minimum of 9 indents separated from each other of ~30 μm were performed on each sample at each strain rate to obtain the average hardness (H) and standard deviations. In order to eliminate indentation size effects and substrate effects, the indentation depth was chosen within 10%–15% of the total thickness of HEA/Cu NTNLs. Besides, the bubble gradient has little influence on the hardness of HEA/Cu NTNLs within

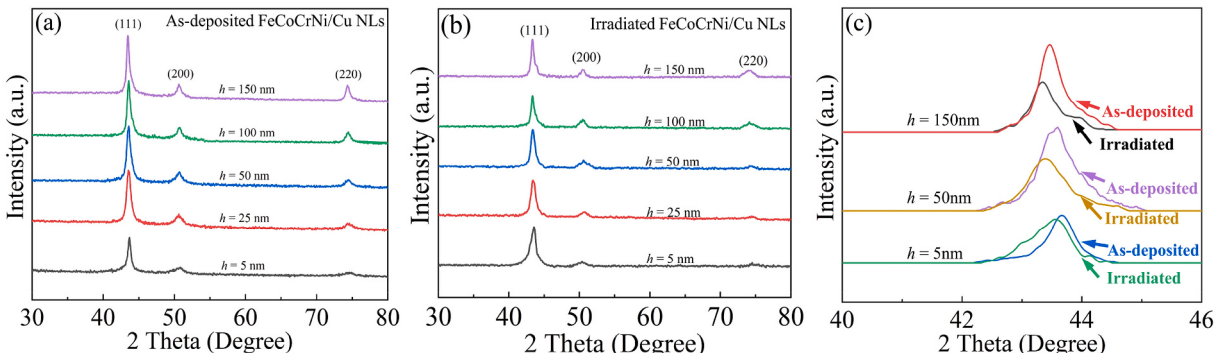


Fig. 1. XRD patterns for HEA/Cu NTNLs with different layer thickness h (a) before and (b) after irradiation. (c) A comparison of XRD profiles between as-deposited and irradiated HEA/Cu NTNLs, showing the change of the (111)-diffraction peak.

this indentation depth-range (Chen et al., 2015; Zhang et al., 2015b). Thus, all the hardness values were measured at the depth of ~ 150 nm for HEA/Cu NTNLs before and after irradiation.

Note that the design of indentation tests was based on the He concentration vs penetration depth profiles via the SRIM calculations (Stoller et al., 2013; Wei et al., 2011). According to the results of SRIM, the highest radiation damage of ~ 4.5 dpa and a maximum He concentration of ~ 8 at. % in the HEA/Cu NTNLs with different h are achieved at the depth of ~ 150 nm. Generally, the NLs with more interfaces (or the h is less than 10 nm) often result in the different position of peak He bubble density between experimental observations and SRIM simulations (Chen et al., 2015; Li et al., 2009), while this difference in the present HEA/Cu NTNLs was not significant, consistent with our previous work (Wu et al., 2018a; Zhang et al., 2015b).

3. Results

3.1. Crystallographic orientations of HEA/Cu NTNLs

High-angle XRD spectra for the as-deposited and irradiated HEA/Cu NTNLs with h spanning from 5 to 150 nm are shown in Fig. 1(a) and (b), respectively. It appears that the as-deposited HEA/Cu NTNLs show a strong (111), weak (200) and (220) textures. The overlapping peaks of Cu and FeCoCrNi is ascribed to their same crystal structure and similar lattice parameters (~ 0.361 nm for Cu and ~ 0.358 nm for FeCoCrNi). Compared with the diffraction angles of bulk Cu and FeCoCrNi alloys (Wang et al., 2012), one can find that the diffraction peaks of HEA/Cu NTNLs are in between those of FeCoCrNi and Cu. For instance, the diffraction angles of the (111) peak of Cu and HEA are 43.3° and 43.9° , respectively, while that of HEA/Cu NTNLs is just 43.6° . Compared with the un-irradiated samples, there is no change in grain orientations of irradiated HEA/Cu NTNLs, as shown in Fig. 1(b). After He-implantation, the intensity of all diffraction peaks decreased without significant peak shift, and the central peak became broader, as shown in Fig. 1(c). These XRD results about the grain orientations are consistent with the results of the selected area diffraction patterns (SADPs) in irradiated regions, as presented below.

3.2. Internal microstructure of un-irradiated HEA/Cu NTNLs

3.2.1. Initial microstructure of as-deposited HEA/Cu NTNLs

The typical cross-sectional TEM images of as-deposited HEA/Cu NTNLs with different h are displayed in Fig. 2. The microstructural

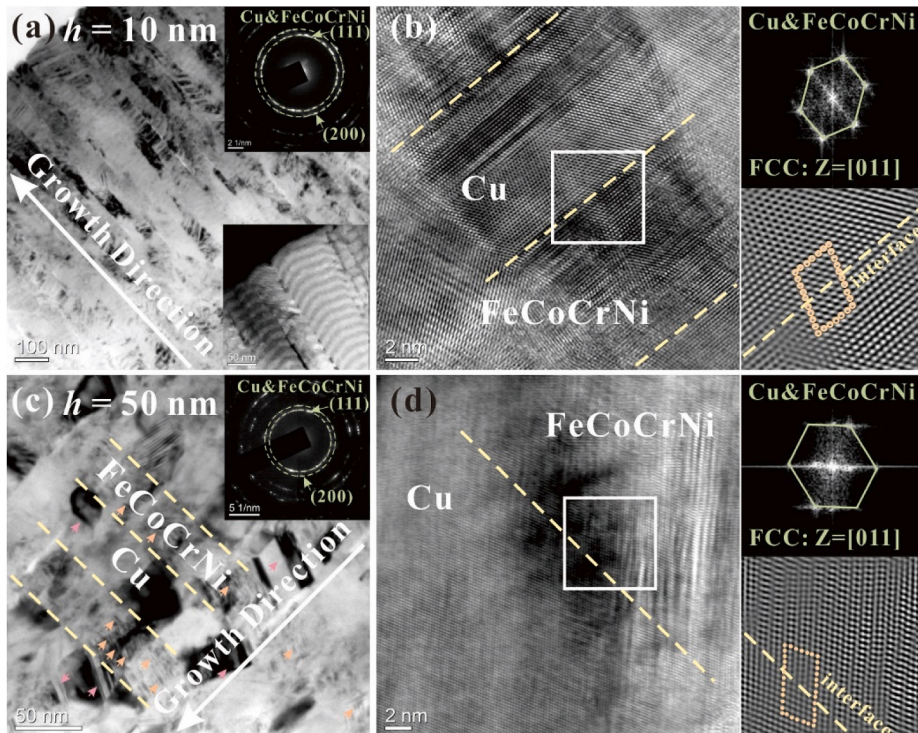


Fig. 2. (a, b) Typical XTEM images of HEA/Cu NTNLs with $h = 10$ nm shows the columnar grains cross interfaces, while the STEM image inserted in (a) shows the modulated structure. (c, d) Typical XTEM images of HEA/Cu NTNLs with $h = 50$ nm show nanolayered structure with coherent interfaces and nanotwins inside the nanograins. The corresponding SADPs inserted in (a, c) exhibit (111) and (200) textures. The corresponding IFFT images of the white boxed regions in (b, d) display the coherent interfaces between Cu and FeCoCrNi HEA layers.

morphologies of HEA/Cu NTNLs can be divided into two regimes by a critical layer thickness of $h_c = 25$ nm. In the Regime-I ($h < h_c$), the HEA/Cu NTNLs show single crystal-like columnar grains along their growth direction with nanotwins penetrated across interfaces (referred as to penetrated nanotwins hereafter), similar to the reported Cu/Ni (Liu et al., 2011) and Cu/330SS (Zhang et al., 2004) NLS with small h . The interfaces could not be discerned in the bright field cross-sectional TEM image, but the STEM image clearly shows a chemical modulation structure, see Fig. 2(a). Thus, HEA and Cu layers have the same grain size (d). The grain size of HEA/Cu NTNLs decreases from ~ 38 to ~ 28 nm with reducing h , as shown in Table 1. A high density of nanotwins and stack faults (SFs) can be observed in both Cu and FeCoCrNi layers, see Fig. 2(b). One can find that the most of segment of layer interfaces are coherent without misfit dislocations.

In the Regime-II ($h \geq h_c$), HEA/Cu NTNLs exhibit the modulated lamella with most of nanowins confined in isolated layers (referred as to confined nanotwins hereafter), see Fig. 2(c). It appears that almost all of nanosized HEA grains contain extremely thin nanotwins, while a relatively lower fraction P^T of Cu grains contain thick nanotwins. The grain sizes of HEA layers are almost constant of ~ 9 nm and insensitive to h , while those of Cu reduce from ~ 55 to ~ 21 nm with decreasing h from 150 to 50 nm. In this regime, the interfaces in HEA/Cu NTNLs with large h are still coherent, see Fig. 2(d). In addition, the SADPs in Fig. 2(a, c) show the overlapping of (111) and (200) rings, implying the coherent interface between HEA and Cu.

The features of growth nanotwins in HEA/Cu NTNLs in terms of the twins' fraction P^T and the twin thickness λ was analyzed, as listed in Table 1. In the Regime-I, the thickness λ almost keeps constant of ~ 5 nm in HEA/Cu NTNLs with nearly constant P^T of $\sim 80\%$. In the Regime-II, the fully NT HEA layers have an identical thickness of $\lambda \sim 2$ nm, while it reduces from ~ 11 to ~ 7 nm in Cu layers with decreasing h , accompanied with the reduced P^T .

3.2.2. Deformed microstructure of as-deposited HEA/Cu NTNLs

Post mortem TEM observations were performed on the indented as-deposited HEA/Cu NTNLs at the loading rate of 0.1 s^{-1} to uncover the deformation mechanisms of constituents, as shown in Figs. 3 and 4. For the HEA/Cu NTNLs with $h = 10$ nm, the penetrated nanotwins of columnar grains are present in the undeformed region, whereas the nanotwins completely disappear in the severely deformed region, as shown in Fig. 3. It implies these penetrated nanotwins in small h samples are unstable and detwinning occurs. By contrast, in the Regime-II, the constituents of HEA and Cu in HEA/Cu NTNLs with $h = 50$ nm manifest different microstructural features after deformation, see Fig. 4. In the deformed region, these confined nanotwins in Cu layers disappear, while a large amount of confined nanotwins and SFs still exist in HEA layers. These findings indicate that (i) compared with the constituent of HEA, thinner Cu layers are more favorable to detwin during plastic deformation, and (ii) the twin morphologies (i.e., penetrated nanotwins vs confined nanotwins) have significant influence on the stability of nanotwins; namely these penetrated nanotwins is more preferred to detwin. The cross-sectional TEM images of HEA/Cu NTNLs show that the layers are bent and approximately follow the contour of the indent without forming a shear band, as shown in Fig. 3(b and c) and 4(b, c). Such relatively uniform deformation in HEA/Cu NTNLs is similar to the case of $h = 20$ nm Cu/Ni NLS with a small interfacial misfit strain $\sim 2.63\%$ (Bhattacharyya et al., 2011), but far different from the shear banding in $h = 50$ nm Cu/Au NLS with the interfacial misfit strain $\sim 12.7\%$ (Li et al., 2017b). Furthermore, Figs. 3(c) and 4(c) show the presence of dislocations at interfaces, which are generated during plastic deformation. The plastic strain estimated from the difference between the measured layer thickness h_M before and after indentation for each constituent layer along the red solid line in Fig. 4(a) is displayed in Fig. 4(d). We further define a parameter $\xi = \sum_{i=1}^n (\Delta h_i / h_M)$ to evaluate the contribution from the constituents of Cu/HEA NTNLs to the total plastic deformation. Unexpectedly, it is found in Fig. 4(d) that the HEA layer makes more contribution to the plastic deformation than Cu. The values of ξ for HEA and Cu are ~ 0.65 and ~ 0.35 , respectively, both of which are almost insensitive to h . It is interesting to find that overall the hard HEA layers contribute more to the total plastic strains, in particular for Cu/HEA NTNLs with larger h under indentation deformation which is in contrary to the belief that the soft phase plays a major role in the plastic deformation of conventional bimetallic NLS. There are two factors contribute to this phenomenon. One is the dislocation

Table 1

Summary of the microstructure sizes in as-deposited and irradiated HEA/Cu NTNLs with different h , such as grain size d , twin thickness λ and twin's fraction P^T .

h (nm)			5	10	25	50	100	150
As-deposited	Grain size d (nm)	d_{all}	28 ± 5	39 ± 6	38 ± 6	–	–	–
		d_{Cu}	–	–	–	21 ± 4	45 ± 5	55 ± 7
		d_{FeCoCrNi}	–	–	–	9 ± 3	10 ± 1	9 ± 2
	Twin's fraction P^T (%)	P^T_{all}	81 ± 5	82 ± 6	79 ± 5	–	–	–
		P^T_{Cu}	–	–	–	48 ± 5	57 ± 5	55 ± 5
		P^T_{HEA}	–	–	–	100	100	100
Irradiated	Twin thickness λ_T (nm)	λ_{all}	5 ± 1	5 ± 1	5 ± 1	–	–	–
		λ_{Cu}	–	–	–	7 ± 2	9 ± 2	11 ± 2
		λ_{HEA}	–	–	–	2 ± 1	2 ± 1	2 ± 1
	Twin's fraction P^T (%)	P^T_{all}	82 ± 4	83 ± 5	78 ± 6	–	–	–
		P^T_{Cu}	–	–	–	49 ± 4	58 ± 6	55 ± 4
		P^T_{HEA}	–	–	–	100	100	100
	Twin thickness λ_T (nm)	λ_{all}	5 ± 1	5 ± 1	5 ± 1	–	–	–
		λ_{Cu}	–	–	–	7 ± 1	8 ± 2	11 ± 2
		λ_{HEA}	–	–	–	2 ± 1	2 ± 1	2 ± 1

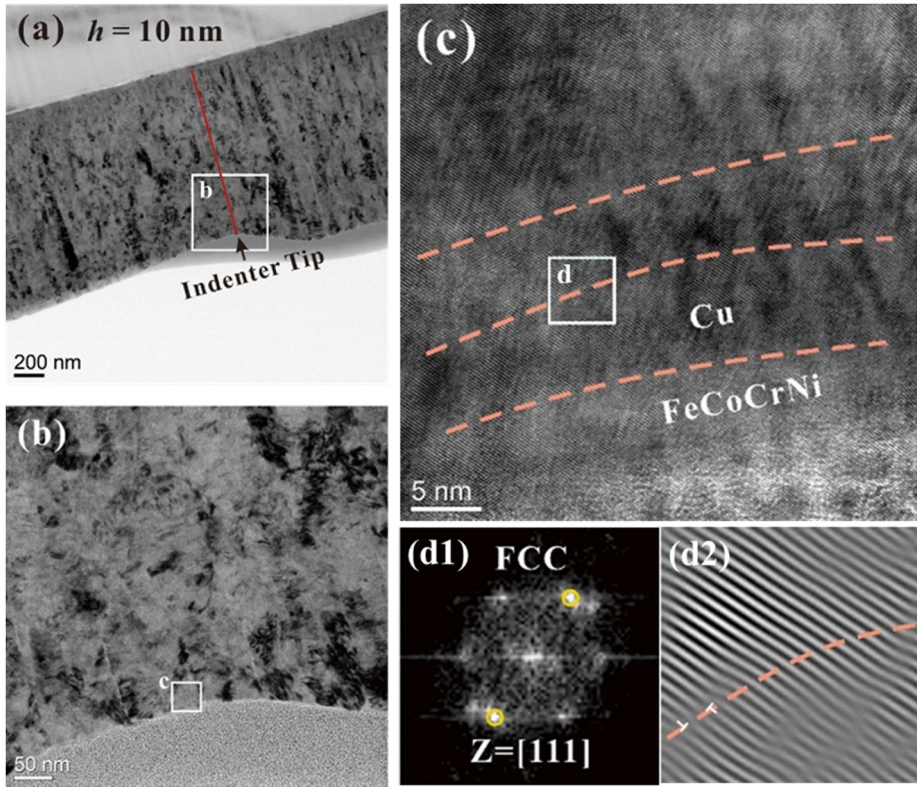


Fig. 3. (a) The typical XTEM image of the indented HEA/Cu NTNLs with $h = 10 \text{ nm}$, showing relatively uniform deformation. (b) The magnified view of the boxed region in (a). (c) The HRTEM image of the boxed region in (b), showing detwinning of penetrated nanotwins. (d1) The corresponding FFT images of the white boxed region in (c). (d2) The corresponding IFFT images of the white boxed region in (c), showing some dislocations at the interface. Dislocations are marked by “ \top ” in the IFFT image.

accumulation in the Cu layer leads to Cu become harder than HEA due to strong strain hardening, and the other one is emitted dislocations from GBs/TBs in the Cu can transmit across the interface into the HEA associated with a higher density of mobile dislocations to cause greater plasticity of HEA. More details can be referred to our previous work (Zhao et al., 2019) and recent atomistic simulations (Feng et al., 2020), and would not be discussed here.

3.3. Internal microstructure of irradiated HEA/Cu NTNLs

3.3.1. Initial microstructure of He ion-irradiated HEA/Cu NTNLs

Extensive TEM observations were conducted to examine the microstructure of He ion-irradiated HEA/Cu NTNLs. Fig. 5(a) is the cross-sectional TEM overview of irradiated HEA/Cu NTNLs with $h = 10 \text{ nm}$, showing a nanolayered structure. The superimposed solid curve presents the depth profile of He concentrations calculated by SRIM. In the peak damage region, high-densities of He bubbles are observed in both HEA and Cu layers, as shown in Fig. 5(b). Also, in the present damage level $< \sim 4.5 \text{ dpa}$, the He bubbles are universally distributed within the layers, thus we have not observed bubble density reduction as a function of distance from the layer interface. After He-implantation, the penetrated nanotwins in both Cu and HEA layers are survived, see Fig. 5(c), without changes in both the twin thickness and the twins’ fraction during He ion-irradiation. Moreover, the (localized) coherent interfaces are still retained in the irradiated region and no change of grain orientation takes place, consistent with the embedded SADPs in Fig. 5(a) and the above XRD results.

The microstructure of irradiated HEA/Cu NTNLs with $h = 50 \text{ nm}$ was also examined. Fig. 6(a) shows a panoramic view of the irradiated specimen incorporating the SRIM simulated depth-dependent profile of He concentrations. Four boxed regions captured at different depths are shown at higher magnifications to uncover the distribution of He bubbles. In the surface region, He bubbles (in Cu) were randomly distributed, see Fig. 6(b). In the peak damage region, high-densities of He bubbles were observed in both Cu and HEA layers, see Fig. 6(c) and (d), respectively. Fewer He bubbles were observed in the HEA layer near the end of the projected ion range, see Fig. 6(e). The average bubble size in Cu is much larger than that in HEA. Still, these confined nanotwins in both Cu and HEA layers survived after He-implantation, without changes in both the twin thickness and the twins’ fraction during He ion-irradiation, as listed in Table 1.

The average diameter (d_{bub}) and spacing (l_{bub}) of He bubbles in Cu layers are presented in Fig. 7(a). It appears that in Cu layers, the

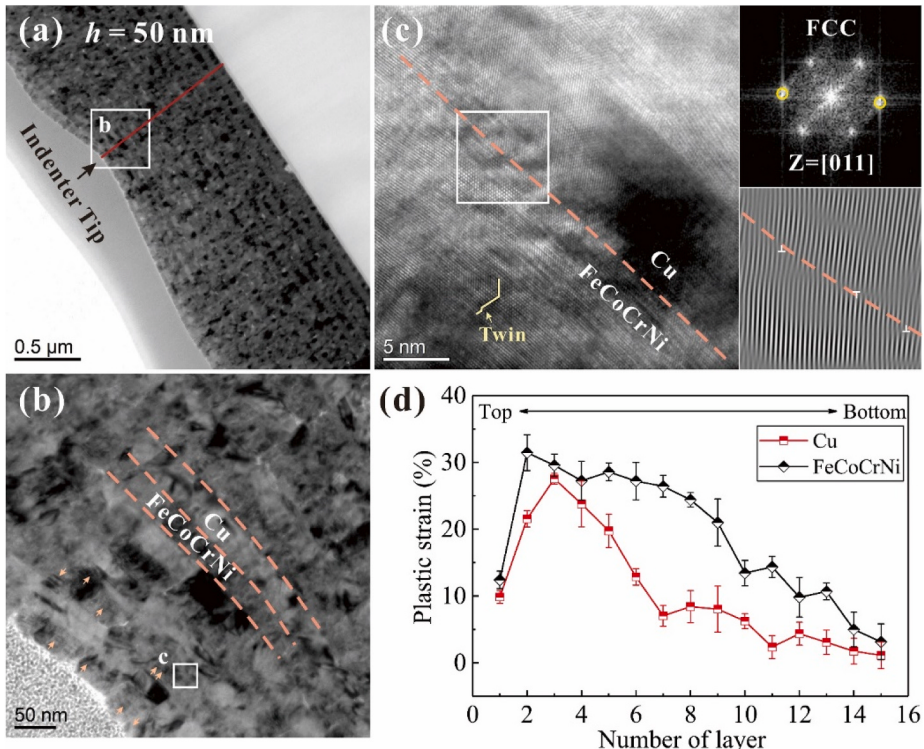


Fig. 4. (a) The typical XTEM image of the indented HEA/Cu NTNLs with $h = 50$ nm, showing relatively uniform deformation. (b) The magnified view of the boxed region in (a). (c) The HRTEM image of the boxed region in (b), showing detwinning of confined nanotwins in Cu. The corresponding FFT and IFFT images of the white boxed region in (c) are displayed, showing some dislocations at the interface. Dislocations are marked by “ \top ” in the IFFT image. (d) The plastic strain as a function of the number of layers for each constituent layer along the line in (a), showing FeCoCrNi HEA layers contribute more to the plastic deformation.

average bubble spacing l_{bub}^{layer} presents a monotonically increased trend with decreasing h (l_{bub} increases from ~ 3.7 to ~ 5.1 nm as h decreases from 150 to 5 nm), and the average diameter d_{bub}^{layer} increases from 2.1 to 3.0 nm with reducing h . Correspondingly, the He bubble density $N_{bub} \approx 1/(l_2 bub d_{bub})$ of Cu layers is significantly reduced by ~ 3 times with reducing h , see Fig. 7(b). By contrast, the average diameter d_{bub} and spacing l_{bub} of He bubbles in HEA layers are much smaller than those in Cu layers, as shown in Fig. 7(c). Since it is difficult to observe He bubbles in the HEA layers with $h = 5$ nm, only the sizes of bubbles in the HEA layers with $h = 10, 25, 50, 100$ and 150 nm were counted (and discussed below). It is found that the average diameter d_{bub} is almost a constant of ~ 1 nm, insensitive to h , while the average spacing l_{bub} decreases from ~ 3.5 to ~ 2.6 nm with reducing h from 150 to 10 nm. Correspondingly, the bubble density N_{bub} increased by ~ 1.5 times as h decreases from 150 to 10 nm, which is much higher than that in Cu layers, see Fig. 7(d).

3.3.2. Deformed microstructure of He ion-irradiated HEA/Cu NTNLs

Post mortem TEM observations were performed on the indented irradiated HEA/Cu NTNLs with $h = 10$ nm in the Regime-I at the loading rate of 0.1 s^{-1} to uncover the deformation mechanisms of constituents, as shown in Fig. 8. For the HEA/Cu NTNLs with $h = 10$ nm, the penetrated nanotwins in single crystal-like columnar grains are still present in the deformed region, see Fig. 8(b1, c1). It implies the penetrated nanotwins are stabilized by He-implantation, so that detwinning would not take place. Meanwhile, these He bubbles within these layers stretch and grow to accommodate deformation since their shape become elongated after indentation, see Fig. 8(b2, c2).

The microstructure of indented irradiated HEA/Cu NTNLs with $h = 50$ nm in the Regime-II was also examined, as shown in Fig. 9. It appears that the confined nanotwins in both HEA and Cu are present in both undeformed and severely deformed regions, as shown in Fig. 9(c-f). It implies that these confined nanotwins are stabilized by He-implantation. Again, these He bubbles within these layers stretch and grow to accommodate deformation after indentation (not shown here). Moreover, the HEA layers contribute more to the plastic deformation than the Cu layers, analogous to the un-irradiated samples, as shown in Fig. 9(b). The parameter ξ for the HEA and Cu are ~ 0.62 and ~ 0.38 , respectively, both of which are almost insensitive to h .

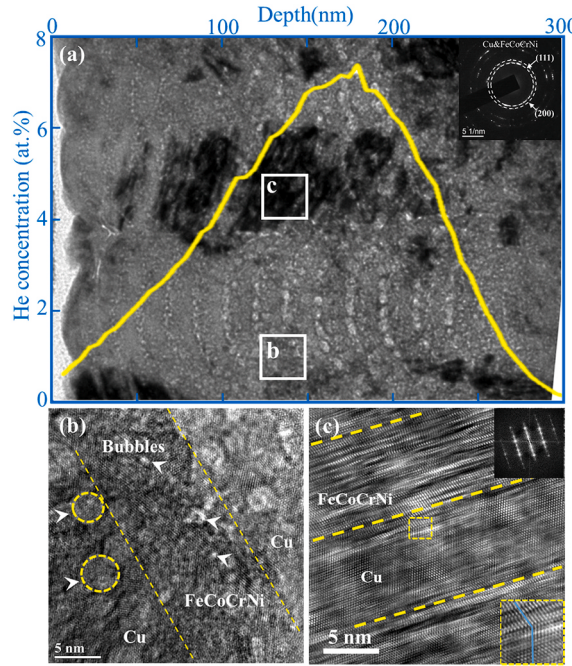


Fig. 5. (a) A typical XTEM image of irradiated HEA/Cu NTNLs $h = 10$ nm with embedded the He concentration profile. The corresponding SADP of the irradiated region shows the unchanged crystallographic orientation of constituents. (b) A HRTEM image of the distribution of He bubbles indicated by white arrows and yellow dashed circle. Images (b) are captured in the condition of under-focus 250 nm to clearly show the He bubbles. (c) A HRTEM image of nanolayered structure with coherent interfaces and nanotwins in irradiated region. (c) are captured in the condition of under-focus 0 nm to clearly show the lattice. The corresponding FFT are displayed, showing the twinning relationship.

3.4. Mechanical properties of HEA/Cu NTNLs

3.4.1. Nanoindentation hardness of HEA/Cu NTNLs

The typical indentation load-depth curves of the as-deposited and irradiated HEA/Cu NTNLs with different h at the same strain rate of 0.05 s^{-1} are displayed in Fig. 10(a) and (b), respectively. It is found that the indentation depth of both the as-deposited and irradiated HEA/Cu NTNLs decreases with reducing h from 150 to 5 nm. Accordingly, the hardness H of as-deposited samples increases from ~ 3.7 to $\sim 5.6 \text{ GPa}$, while that of irradiated samples increases from ~ 4.7 to $\sim 6.6 \text{ GPa}$, as shown in Fig. 10(c). Although both as-deposited and irradiated samples exhibit the fashion that smaller h leads to higher hardness, the HEA/Cu NTNLs exhibit a unusual irradiation hardening behavior associated with the minimum increment of $\sim 0.6 \text{ GPa}$ at $h = 10$ nm, as shown in Fig. 10(d). Above this size of $h = 10$ nm, the hardness increment decreases with reducing h . This phenomenon was also observed in the incoherent system of Mo/Cu (Zhang et al., 2016), V/Cu (Wei et al., 2019), V/Ag (Zhang et al., 2015a) and Ni/Ag (Yu et al., 2013b) NLs and the crystalline/amorphous system of Cu/Zr NLs (Liang et al., 2019), as shown in Fig. 11. While below this size, the irradiation hardening increases with further reducing h , similar to the coherent Cu/Co NLs (Chen et al., 2015), see Fig. 11.

3.4.2. Strain rate sensitivity of HEA/Cu NTNLs

Fig. 12(a) and (b) present the strain rate-dependent hardness of as-deposited and irradiated HEA/Cu NTNLs, respectively, in which the slope represents SRS index m and is summarized in Fig. 12(c). Although the hardness increases with increasing the strain rate, it unexpectedly appears that as decreasing h the SRS m of HEA/Cu NTNLs decreases from 0.04 at $h = 150$ nm in the Regime-II to 0.005 at $h = 5$ nm in the Regime-I. This is contrary to the general findings in FCC pure metals, such as Cu (Cheng et al., 2005; Shen et al., 2006) and Ni (Dalla Torre et al., 2005; Wang et al., 2006), whose SRS m (>0) monotonically increases with decreasing the grain size. This monotonically size-dependent SRS m of the as-deposited HEA/Cu NTNLs is far different from the reported Cu/Ni NLs (Liu et al., 2019) with a maximum SRS m at $h = 25$ nm, which is cause by the coherent to semi-coherent interfacial transition at this critical size (Liu et al., 2019). Also, the present as-deposited HEA/Cu NTNLs behave different from the reported as-deposited NLs with monotonically increased SRS m with decreasing h , such as Cu/Zr (Zhang et al., 2014a), Mo/Zr (Wu et al., 2018a), Cu/Mo (Zhang et al., 2016) and Cu/Cr (Zhang et al., 2014a), as shown in Fig. 12(d). After He + irradiation, the SRS m of as-deposited HEA/Cu NTNLs sharply reduces. Moreover, the SRS m of irradiated HEA/Cu NTNLs also unexpectedly decreases from 0.002 to -0.015 as h reduces from 100 to 5 nm. Under the same fluence of $1 \times 10^{17} \text{ ions} \cdot \text{cm}^{-2}$, it is found that both irradiated Cu/Mo and Zr/Mo NLs exhibit the positive SRS m . They first exhibit decreased SRS m , reaching the minimum SRS ($m \sim 0.028$ for Cu/Mo; $m \sim 0.012$ for Zr/Mo) at a critical h of ~ 50 nm, and then exhibit increased SRS m with further decreasing h , see Fig. 12(d).

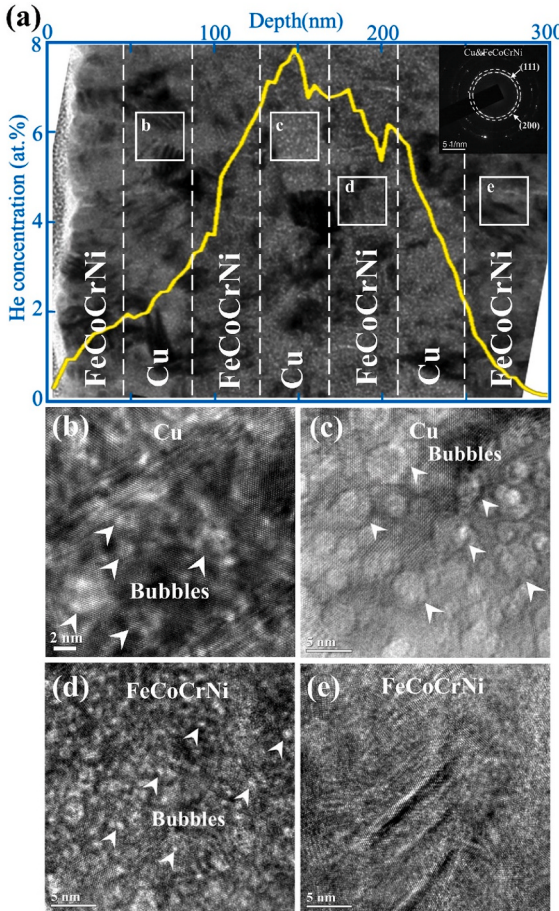


Fig. 6. (a) A typical XTEM image of irradiated HEA/Cu NTNLs $h = 50$ nm with embedded the He concentration profile. The corresponding SADPs inserted in (a) exhibit (111) and (200) textures. (b-e) display the HRTEM images of the boxes b–e labeled in (a) at different penetration depths. Bubbles were randomly distributed in (b, c) Cu and (d) FeCoCrNi HEA layers. (e) Fewer He bubbles were observed in the FeCoCrNi HEA layer. Images (b–e) are captured in the condition of under-focus 250 nm to clearly show the He bubbles.

4. Discussion

4.1. The interface density effects on the He ion-irradiation-induced damage

Previous studies showed that in He ion-irradiated conventional (nontwinned) bimetal multilayers, such as Ag/Ni (Yu et al., 2013b), Mo/Cu (Zhang et al., 2016), V/Ag (Zhang et al., 2015a) and V/Cu (Fu et al., 2010), the He bubble density N_{bub} (or increased l_{bub}) in each constituents often decreases with reducing h . The origin of reduced N_{bub} with decreasing h can be ascribed to the interfaces as effective sinks by trapping and annihilating irradiation-induced defects and absorbing He atoms (Demkowicz et al., 2008; Kashinath et al., 2013). This is far different from the CG metals, in which the solubility of He is typically very low, thus a majority of He atoms will enter into vacancy clusters and form pressurized He bubbles. Nanolaminates with smaller h can provide more interfaces and a greater density of misfit dislocations, and hence are more effective to manage He atoms. Therefore, the size dependent reduction of He bubble density was observed in these He ion irradiated systems mentioned above. Moreover, since these BCC metals usually have higher melting temperature and better radiation resistances associated with lower mobility of defects than FCC metals, thus these conventional FCC/BCC bimetal NLs show greater radiation tolerance than their FCC counterparts (Beyerlein et al., 2015).

However, in the present HEA/Cu NTNLs, unlike the constituent Cu with large bubble sizes d_{bub} (>2 nm) and increased spacing l_{bub} , the nearly constant bubble sizes d_{bub} in HEA layers ($h \geq 10$ nm) are very small on the order of ~ 1 nm, with reduced spacing l_{bub} as decreasing h . Even no He bubbles were observed in the HEA layers with $h = 5$ nm. These results indicate that, compared with Cu, fewer vacancies produced per cascade in HEAs, rendering lower probability for clustering of vacancies in HEAs, and lower mobility of trapped He at ambient temperatures in the HEA (sluggish growth of He bubbles) [28]. It means the HEA/Cu interface under such radiation conditions actually only interact with a defect flux from the Cu layer, far different from that of conventional FCC/FCC bimetal NLs, such as Ag/Ni (Yu et al., 2013b). Therefore, Cu layers have larger He bubble sizes with higher spacing, while HEA layers have smaller bubbles with lower spacing. The difference between bubble formation in HEA and Cu, which is similar to the reported

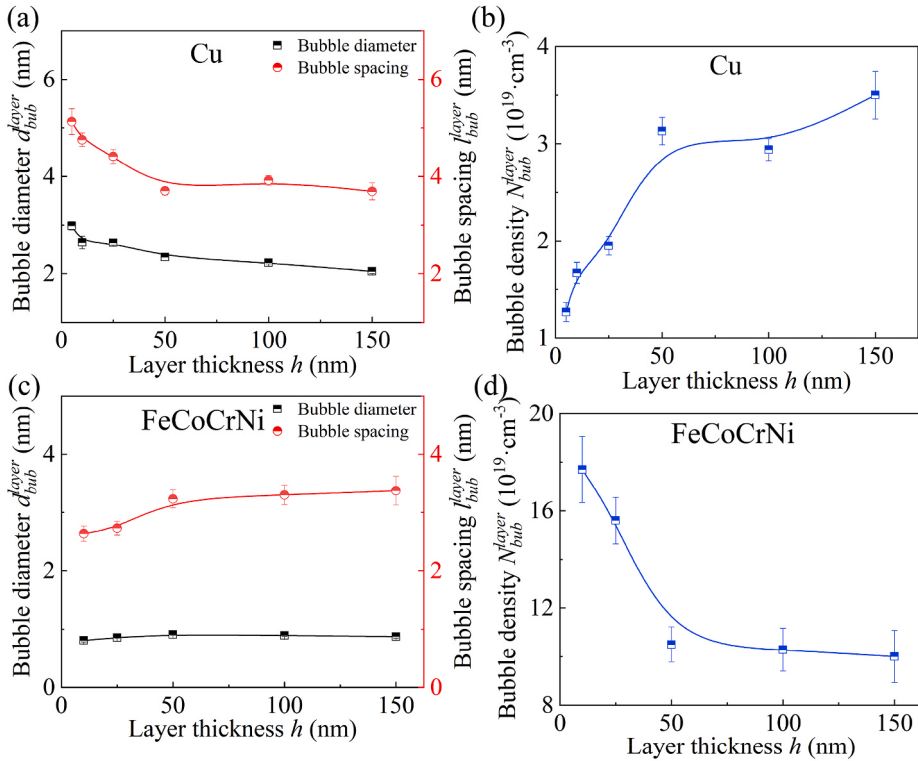


Fig. 7. Statistical results on the parameters of He bubbles in the irradiated HEA/Cu NTNLs. The average bubble diameter and bubble spacing, bubble density as a function of h in Cu layers are shown in (a) and (b), respectively. Similarly, the average bubble diameter and bubble spacing, bubble density as a function of h in FeCoCrNi HEA layers are shown in (c) and (d), respectively.

BCC/FCC system (e.g. Mo/Cu (Zhang et al., 2016), V/Ag (Zhang et al., 2015a) and V/Cu (Fu et al., 2010)), can be attributed to the tailored interstitial defect cluster motion in the alloys from a long-range 1D mode in pure metals to a short-range 3D mode in HEAs, which in turn leads to their enhanced point defect recombination. In other words, the short-range 3D motion of interstitial clusters that significantly increases the vacancy–interstitial recombination rate plays a key role in preventing He bubble formation. The underlying reason is that the high-level site-to-site lattice distortions and compositional complexities in HEAs can be effectively used to modify formation energies, migration barriers and diffusion pathways of irradiation-induced defects, thereby modifying defect generation, interaction, interstitial–vacancy recombination in the early stage of irradiation (Lu et al., 2016; Yang et al., 2017). Consequently, the He bubble density N_{bub} in Cu follows the general trend mentioned above, while that in HEA layers behave the opposite way associated with the size dependent increased He bubble density.

4.2. Deformation mechanisms and He ion-irradiation effects on nanotwins

In the un-irradiated samples, these small nanotwins in both Cu and HEA layers (in the Regime-I) detwin during indentation tests. Previous studies (Fan et al., 2019a) about the stability of nanotwins in un-irradiated Cu have shown that extremely small nanotwins are unstable during plastic deformation. The underlying mechanism is that when the detwinning partials nucleated from the boundaries in NC Cu glide parallel to the TB, these nanotwins would disappear. Prior work (Asaro and Suresh, 2005) has revealed that the deformation mechanism transits from partial to full dislocations nucleated from GBs in Cu at a critical size d_c , given by:

$$d_c = \frac{\eta}{\eta - 1} \cdot \frac{\mu(3s - 1)b_f^2}{3\gamma}, \quad (1a)$$

where $s \sim 2-4$ is a stress factor, μ is the shear modulus, η is the ratio of grain size to equilibrium stacking fault width and $\eta/(\eta-1) \approx 1$, γ is the SFE, b_f is the magnitude of the Burgers vector of the full dislocations. Taking the following parameters: $s = 3$, $\mu_{Cu} = 48.3$ GPa, $\mu_{HEA} = 84$ GPa, $b_{f,Cu} = 0.2556$ nm, $b_{f,HEA} = 0.2524$ nm, $\gamma_{Cu} = 41 \text{ mJ. m}^{-2}$, $\gamma_{HEA} = 30 \text{ mJ. m}^{-2}$, the estimated critical size d_c is about ~ 128.3 and ~ 29.7 nm for Cu and HEA layers, respectively. The calculated critical size d_c is far larger than the characteristic size of the corresponding constituent in HEA/Cu NTNLs, implying partial emission from boundaries is the dominant deformation mechanism. Moreover, the critical stress for partials emission from GBs in constituent layers could be predicted by (Asaro and Suresh, 2005):

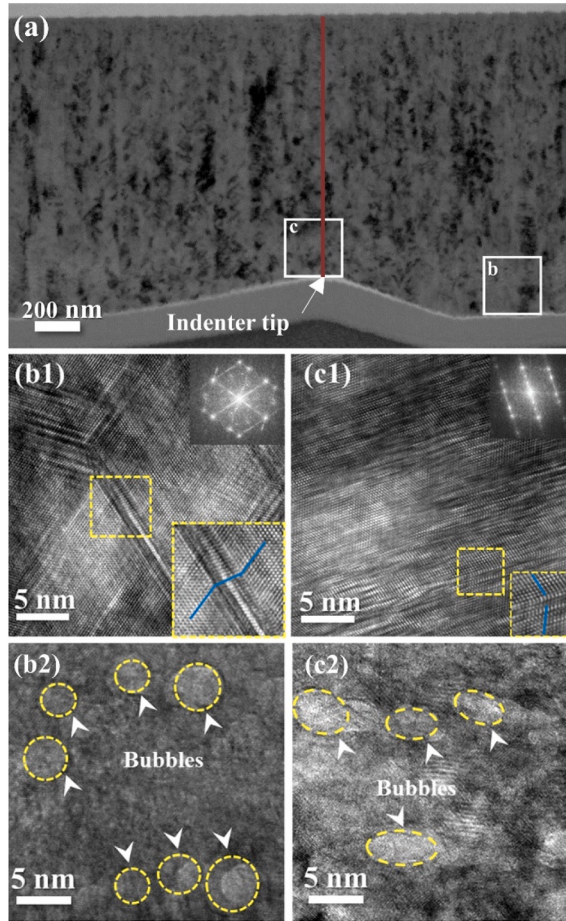


Fig. 8. (a) The typical XTEM image of the irradiated HEA/Cu NTNLs with $h = 10$ nm, showing relatively uniform deformation without shear banding. (b1), (c1) showing the HRTEM image of nanotwins in (b) undeformed and (c) deformed region in (a), respectively. (b2), (c2) showing the He bubbles in (b) undeformed and (c) deformed region in (a), respectively. The corresponding FFT are displayed, showing the twinning relationship.

$$\tau = \frac{\eta - 1}{\eta} \frac{\gamma}{b_f} + \frac{1}{3} \frac{\mu b_f}{d}, \quad (1b)$$

Therefore, using the grain sizes of constituents listed in Table 1, it is found that the needed stress for emission of partials from boundaries is much higher in HEA layers than that of Cu. It is suggested that plastic deformation initiates in the soft Cu, associated with detwinning in Cu. Specifically, the extremely small nanotwins in Cu (with thickness less than ~ 15 nm) promote nucleation of partials from TB-GB conjunctions, rendering dislocation nucleation-controlled softening of NT materials (Li et al., 2010; Wang et al., 2010). A similar result was observed in NT Ni (Li et al., 2016b). It should be pointed out that the in-plane grain sizes of columnar HEA grains are very small, so that the large height-to-diameter ratio of grains (on the order of 50 nm/9 nm = 5.5) makes it difficult to activate the GB-mediated mechanisms under the strong constraining effect caused by interfaces and GBs.

After He-implantation, these nanotwins (in Cu as well as in HEA) survive in the He ion-irradiated HEA/Cu NTNLs after indentation. This finding indicates that the He ion-irradiation induced defects (e.g. He atoms/clusters, bubbles) can notably stabilize these fine nanotwins with thickness of several nanometers during plastic deformation. Although the classical solute drag effect assumes that solute atoms migrate together with GBs, the solute atoms can pin the GBs and reduce their mobility. Specifically, these He defects are in general difficult to move and effectively pin the TBs as well as the GBs, which benefits to stabilize the initial microstructure of HEA/Cu NTNLs. Recent work (Yu et al., 2013a) about *in-situ* Kr ion irradiation studies has shown that the defect size and density in Ag₉₉Fe₁ are significantly reduced comparing with monolithic CG Ag and NT Ag. Also, these extremely fine nanotwins with thickness of ~ 3 nm survived during heavy ion irradiations, because Fe solutes stabilize nanotwins by pinning TBs and thus improve the energy barrier for migration of TBs. This result also indicates that the solute atoms can stabilize the microstructure of alloyed materials. Similarly, the He atoms/clusters at TBs may retard detwinning and enhance strengthening in NT HEA/Cu NTNLs further. More specific, the bubbles with higher pinning strength than He atoms/clusters can more effectively prevent the detwinning process by hindering the twining dislocations to glide on TBs (Fan et al., 2019a). Thus, these nanotwins are difficult to detwin in the He ion-irradiated HEA/Cu samples during indentation tests, and make more contributions to the enhanced hardness of irradiated HEA/Cu samples.

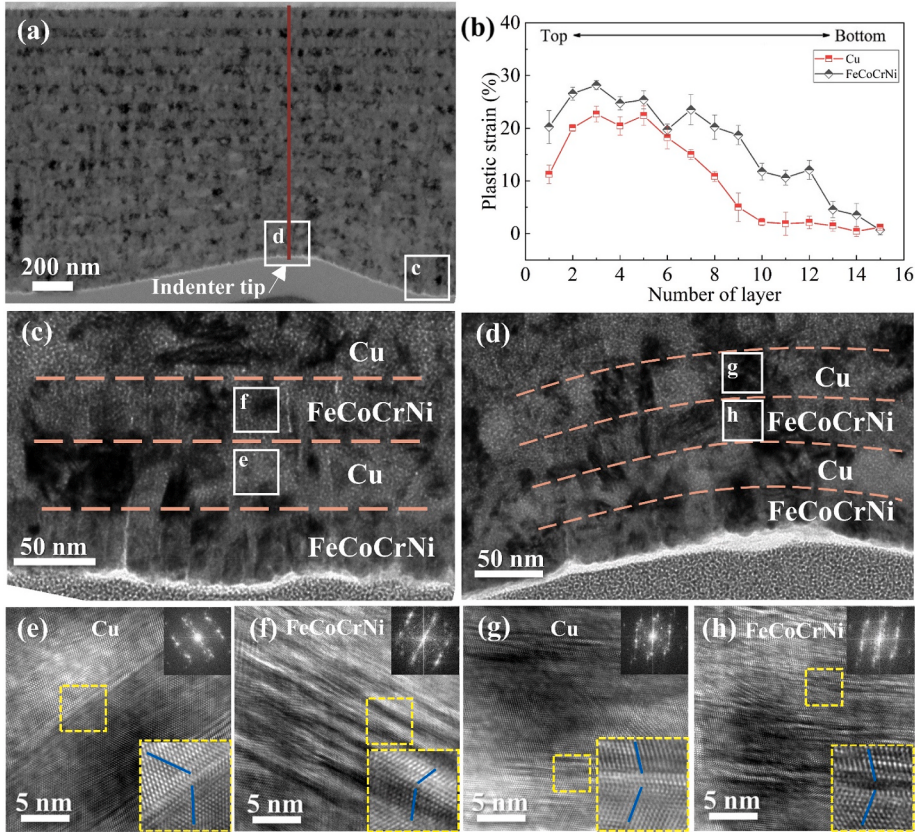


Fig. 9. (a) The typical XTEM image of the irradiated HEA/Cu NTNLs with $h = 50$ nm, showing relatively uniform deformation without shear banding. (b) The plastic strain as a function of the number of layers for each constituent layer along the red solid line in (a), showing FeCoCrNi HEA layers contribute more to the plastic deformation. (c, d) The magnified images of the boxed regions in (a). (e, g) The HRTEM images showing nanotwins in the Cu layer in (c) undeformed and (d) deformed regions, respectively. (f, h) The HRTEM images showing nanotwins in the FeCoCrNi HEA layer in (c) undeformed and (d) deformed regions, respectively. The corresponding FFT images of (e-h) are displayed, showing the twinning relationship.

4.3. Size-dependent hardness and strengthening mechanisms

4.3.1. As-deposited HEA/Cu NTNLs

As mentioned above, the partial-mediated deformation mechanism governs the plastic deformation behavior of HEA/Cu NTNLs. The size-dependent hardness of NLs with $h \geq 50$ nm is widely captured by the Hall-Petch model based on dislocations pile up against a interface. Actually, prior studies (Chen et al., 2012; Zhang et al., 2017; Liu et al., 2011; Misra et al., 2005) have pointed out that the premise for dislocations pile-up in the soft constituent of NLs is that the applied shear stress (τ) less than one half of the IBS to slip transmission (τ_{int}) so that dislocations (with the number of $N > 2$) can pile up against the interface in a slip plane, i.e., $N \cdot \tau \leq \tau_{int}$. For the present HEA/Cu NTNLs with coherent interfaces, the IBS is calculated to be $\tau_{int} \sim 0.69$ GPa via the following equation (Koehler, 1970; Liu et al., 2013):

$$\tau_{int} = \tau_k + \tau_{ch} = \mu_1^* R_1 \frac{\sin \phi}{8\pi} + \frac{\Delta\gamma}{b_p}, \quad (2)$$

where the first term τ_k is the Koehler stress, arises from the modulus mismatch, $\mu_1^* = 2 \frac{\mu_{Cu} \cdot \mu_{HEA}}{\mu_{Cu} + \mu_{HEA}}$ is the mean shear modulus of HEA/Cu NTNLs, $R_1 = \frac{\mu_{HEA} - \mu_{Cu}}{\mu_{HEA} + \mu_{Cu}}$, ϕ is the angle between the slip plane and the interface, and the second term τ_{ch} is a consequence of differences in stacking fault energy (SFE) of the constituents, $\Delta\gamma = \gamma_{Cu} - \gamma_{HEA}$ is the SFE difference, b_p is the magnitude of the Burgers vector of a partial. Taking $\mu_{HEA} = 84$ GPa (Varvenne et al., 2016), $\gamma_{HEA} = 30 \text{ mJ. m}^{-2}$ (Varvenne et al., 2016), $b_{p,Cu} = 0.1457$ nm, the estimated interfacial strength is ~ 2.15 GPa or the peak hardness is ~ 5.8 GPa. Given the hardness H of HEA/Cu NTNLs is in the range of ~ 3.7 – 5.5 GPa, dislocations (with a number of $N \geq 2$) cannot pile up in Cu due to the low strength of coherent interfaces. Once there are more gliding dislocations (with a number of $N > 1$) on the same slip plane, the leading dislocation in Cu would easily transmit across the coherent interface into HEA. In other words, the NT Cu layers without dislocations pile-up likely serve as the dislocation donator and export abundance of dislocations into the HEA acceptor. This scenario was previously verified by *in-situ* TEM observations in Cu/Ni NLs

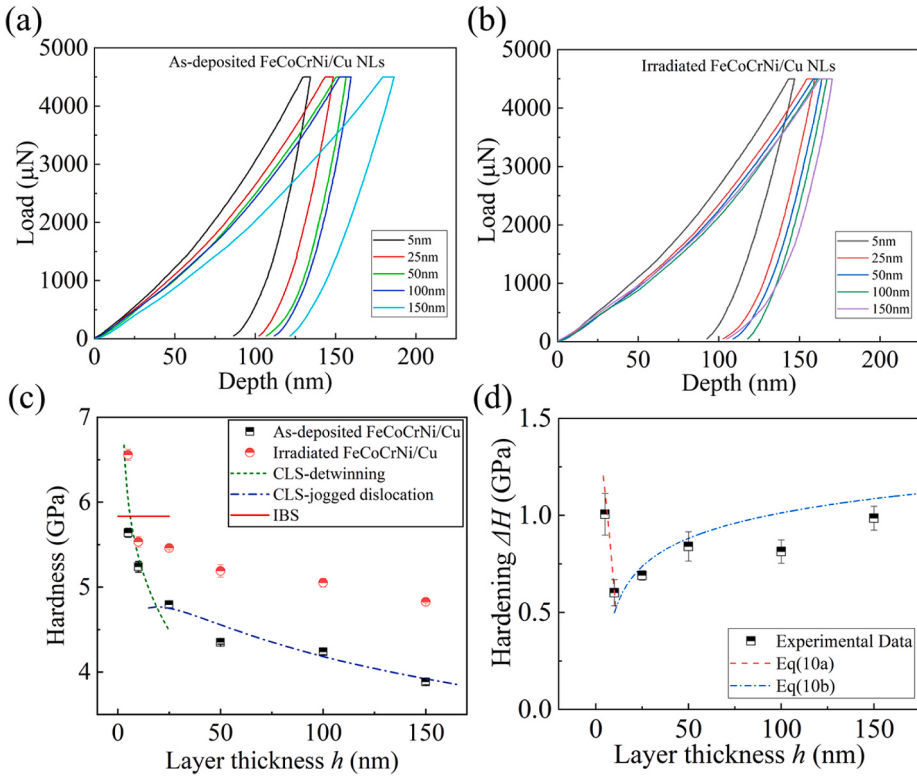


Fig. 10. The load-depth curves of (a) as-deposited and (b) irradiated HEA/Cu NTNLs at the strain rate of 0.05 s^{-1} with different h . (c) The dependence of hardness H on the layer thickness h for both as-deposited and irradiated HEA/Cu NTNLs, showing small h leads to higher H . Also the hardness is analyzed by different models, and more details can be referred to the text. (d) The irradiation hardening ΔH as a function of h , which is quantitatively captured by the mechanistic models, see the text.

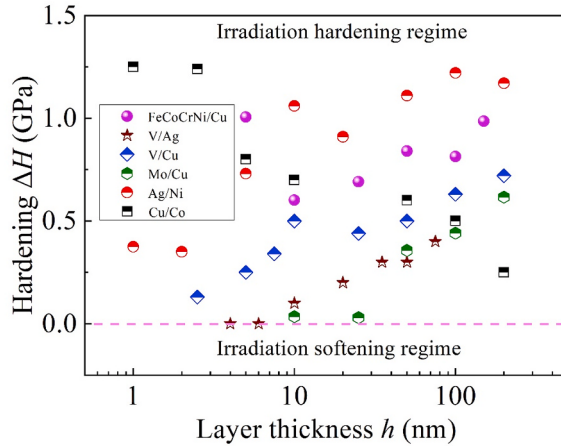


Fig. 11. A comparison of the irradiation hardening as function of h between the present HEA/Cu NTNLs and conventional bimetal systems such as Mo/Cu (Zhang et al., 2016), V/Cu (Wei et al., 2019), V/Ag (Zhang et al., 2015a), Ni/Ag (Yu et al., 2013b) and Cu/Co (Chen et al., 2015).

(Anderson et al., 1999). Also, most recent atomistic simulations (Feng et al., 2020) based on the present microstructure of HEA/Cu NTNLs showed that when these partial dislocations in Cu propagate through the interface, they can slip freely in HEA layer, rendering their good plasticity. As a result, Cu and HEA layers co-deform to a large magnitude of plastic strains.

In the HEA/Cu NTNLs, dislocation emission from boundaries is not a problem; while nanotwins render dislocation motion confined in isolated layers becomes difficult. Thus, if the dislocation gliding stress is less than the IBS, it would propagate in a confined layer. Misra et al. (2005) proposed a refined CLS model considering the effect of dislocation core spreading along the interface, interface

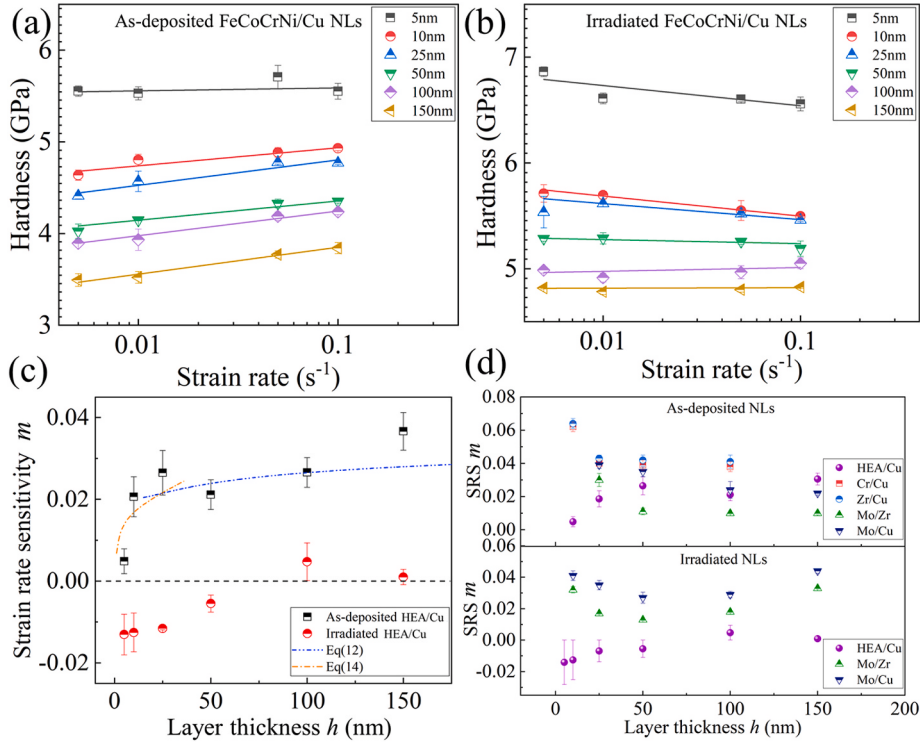


Fig. 12. (a) The measured hardness H as a function of strain rate for (a) as-deposited and (b) irradiated HEA/Cu NTNLs with different h . (c) The measured strain rate sensitivity (SRS) index m of as-deposited and irradiated HEA/Cu NTNLs. The positive SRS m of the as-deposited HEA/Cu NTNLs is quantitatively captured in different size regimes by the dislocation models. (d) A comparison of the size-dependent SRS m among the present HEA/Cu NTNLs and other reported nontwinned NLs such as Cu/Mo (Zhang et al., 2016), Mo/Zr (Wu et al., 2018a), Cu/Zr (Zhang et al., 2014a) and Cu/Cr (Zhang et al., 2014a) before and after irradiation.

stress and resistance from interface dislocation arrays, as follows:

$$\sigma_{CLS} = \frac{M\mu b_p \sin \phi}{8\pi h} \left(\frac{4-\nu}{1-\nu} \right) \ln \left(\frac{\alpha h}{b_p \sin \phi} \right) - \frac{F}{h} + \frac{\mu f \varepsilon}{B(1-\nu)}, \quad (3a)$$

where M is Taylor factor, ν is poisson's ratio, α represents the core cut-off parameter, F is the characteristic interface stress of C/CNLS, f is volume fraction of constituent layers, ε is the in-plane plastic strain, B is a strain resolution factor of ~ 0.5 for the active slip system. Considering the polycrystalline nature of constituents as well as their lattice friction stresses in HEA/Cu NTNLs, we replace h with the effective characteristic size $h^* = (2d + h)/3$ (Colla et al., 2012). In such a case, Eq. (3a) can be modified as:

$$\sigma_{CLS}^* = \frac{M\mu b_p \sin \phi}{8\pi h^*} \left(\frac{4-\nu}{1-\nu} \right) \ln \left(\frac{\alpha h^*}{b_p \sin \phi} \right) - \frac{F}{h^*} + \frac{\mu f \varepsilon}{B(1-\nu)} + \sigma_0, \quad (3b)$$

where σ_0 represents the friction stress which reflects the essential characteristic of a material. As for Cu, σ_0 is very small so that it can be neglected. For FeCoCrNi, the intrinsic lattice stress can be predicted by a new solute strengthening theory based on the concept of misfit volume ΔV_n in HEAs (Varvenne et al., 2017), as below:

$$\tau_0 = A_c \zeta^{-\frac{1}{3}} \mu \left[\frac{1 + \nu_{alloy}}{1 - \nu_{alloy}} \right]^{\frac{1}{3}} \left[\frac{\sum_n c_n \Delta V_n^2}{b_f^6} \right]^{\frac{2}{3}}, \quad (3c)$$

$$\Delta E_b = A_E \zeta^{\frac{1}{3}} \mu b_f^3 \left[\frac{1 + \nu_{alloy}}{1 - \nu_{alloy}} \right]^{\frac{2}{3}} \left[\frac{\sum_n c_n \Delta V_n^2}{b_f^6} \right]^{\frac{1}{3}}, \quad (3d)$$

$$\sigma_0(T, \dot{\varepsilon}) = 3.06 \tau_0 \left[1 - \left(\frac{k_B T}{\Delta E_b} \ln \frac{\dot{\varepsilon}_D}{\dot{\varepsilon}} \right)^{\frac{1}{3}} \right], \quad (3e)$$

where ΔV_n is the misfit volumes of each type elements, c_n is the molar percent of component, k_B is the Boltzman constant, T is the temperature and $\dot{\epsilon}$ is the strain rate. Taking the parameters: $A_r = 0.01785$, $A_E = 1.5618$ for fcc alloys and $\varsigma = 0.125$, we can obtained σ_0 of FeCoCrNi at 300 K is ~ 109 MPa (Varvenne et al., 2017). However, this modified CLS model, i.e., Eq. (3b) ignores the contribution of nanotwins and SFE, which have significant effects on the strengthening behavior of HEA/Cu NTNLs.

Because the microstructural evolution is quite different in Regime-I and Regime-II, in what follows, we respectively discuss the strengthening behavior in these two regimes to further refine Eq. (3). In the Regime-I with $h < h_c$, it is found that detwinning occurs in nanosized columnar grains, owing to interactions between nanotwins and gliding partials (Li et al., 2016b; Wang et al., 2010). In fact, the CLS model mentioned above neglects this interaction (dedicated to detwinning) and the SFE effect on gliding partials that induces a back stress due to the SF behind a leading partial in non-twinned grains. Thus, considering the effect of detwinning in twinned grains and the back stress in non-twinned grains, the estimated strength can be expressed as (Li et al., 2010, 2016a):

$$\sigma_{CLS}^* = \sigma_{CLS}^m + P^T M \left[\frac{\Delta U}{SV^*} - \bar{SV}^* \ln \frac{d}{\lambda} \frac{\nu_D}{\dot{\epsilon}} \right] + (1 - P^T) M \frac{\gamma}{b_p} \quad (4)$$

where ΔU is the activation energy, S is a factor representing local stress concentration and geometry, V^* is the activation volume, ν_D is the Debye frequency, other symbols have the same meaning before. Because the constituents of HEA/Cu NTNLs co-deform, we approximately estimate the hardness as follows (Fan et al., 2017):

$$H = 2.7 (\xi_{Cu} \cdot \sigma_{Cu}^* + \xi_{HEA} \cdot \sigma_{HEA}), \quad (5)$$

where σ_{Cu}^* and σ_{HEA}^* are the strength of Cu and HEA, respectively, which can be estimated by Eq. (4). Taking $\xi_{Cu} = 0.35$, $\xi_{HEA} = 0.65$, $M = 3$, $\nu_{Cu} = 0.343$, $\nu_{HEA} = 0.28$ (Varvenne et al., 2016), $b_{p,HEA} = 0.1457$ nm, $\alpha_{Cu} = 0.01$, $\alpha_{HEA} = 0.004$, $F = 2$ J m⁻² (Misra et al., 2005), $\varepsilon_{Cu} = 0.9\%$, $\varepsilon_{HEA} = 1.7\%$, $\Delta U = 1.0$ eV (Li et al., 2010), $S = 0.33$ (Li et al., 2010), $\nu_D = 1.3 \times 10^{13}$ s⁻¹, $k_B = 1.38 \times 10^{-23}$ J K⁻¹, $T = 298$ K, $\dot{\epsilon} = 0.05$ s⁻¹ and $V^* = b_p \chi l^* = b_p^2 l^* = \psi b_p^2 h^*$, where χ is the distance (of the order of b_p) swept out by the mobile dislocation during an activation event, l^* is the effective dislocation segment length involved in a local activation event and scales with the effective size h^* , and ψ is a proportionality factor. Substituting Eq. (4) into Eq. (5), the calculated hardness agrees well with experimental data in the Regime-I, see the black line in Fig. 10(c).

However, the deformation mechanism changes as h increases into the Regime-II based on our TEM observations. The calculated hardness of the HEA/Cu NTNLs with large $h > 25$ nm from above equations far underestimates the experimental data. This can be ascribed to the maintenance of nanotwins in HEA layers during deformation and the transition from hairpin-like to multiple jogged necklace-like motion when λ is less than ~ 3 - 4 nm (Zhu et al., 2015). In this regard, the CLS model for the FeCoCrNi HEA can be modified as (Zhou et al., 2014).

$$\sigma_{HEA} = \sigma_{CLS}^m + M f_{pin} \frac{1}{b_f \lambda}, \quad (6)$$

where f_{pin} is the pinning force exerted by TBs, other symbols have the same meaning above. In this regime, detwinning also occurs in Cu layers, so that Eq. (4) is still applicable. Taking $b_{f,HEA} = 0.2524$ nm, $f_{pin} = 0.03$ μ N (Zhou et al., 2014), the estimated hardness agrees well with the experimental data, as shown in Fig. 10(c).

4.3.2. Irradiated HEA/Cu NTNLs

Based on above results and discussion, the irradiation hardening is mainly resulted from two aspects, i.e., the stabilized nanotwins and He bubbles inside the constituent layers. Because the solubility of He in most nuclear metals is negligible as mentioned earlier, the accumulation of He atoms in metals after irradiation is usually accompanied by abundant defect clusters/bubbles, rendering these nanotwins is stabilized by these He defects in irradiated HEA/Cu NTNLs. For the sake of simplicity, we neglect the effects of He defects on the lattice distortion or the friction stress, and only consider the effects of the stabilized nanotwins and He bubbles on the irradiation hardening of HEA/Cu NTNLs. In this case, the hardness increment caused by the difference between the stress required for partial emission and the detwinning stress can be expressed as:

$$\Delta H_{twin} = 2.7 \cdot M \left\{ \frac{1}{s} \left(\frac{\eta - 1}{\eta} \cdot \frac{\gamma}{b_f} + \frac{\mu b_f}{3\lambda} \right) - \left[\frac{\Delta U}{SV^*} - \frac{k_B T}{SV^*} \ln \left(\frac{d}{\lambda} \frac{\nu_D}{\dot{\epsilon}} \right) \right] \right\} \cdot P^T, \quad (7)$$

where the symbols have the same meaning as above. On the other hand, the dispersed bubble hardening is frequently used to describe the strengthening effect in light of the weak pinning effect of He bubbles on gliding dislocations, based on the Orowan model. Accordingly, the increased hardness (ΔH_{bubble}) caused by bubbles in NLS can be given as follows by considering the equilibrium between line force and resistance of all bubbles over the length (Wei et al., 2011)

$$\Delta H_{bubble} = 2.7 M \tau_i \left(1 - \frac{l_{bub}^{layer}}{\sqrt{2}h} \right), \quad (8)$$

where τ_i is the average shear strength of bubbles, l_{bub}^{layer} is the average bubble spacing.

Taken together, the total irradiation hardening can be given by:

$$\Delta H_{\text{irradiation}} = \Delta H_{\text{twin}} + \Delta H_{\text{bubble}}. \quad (9)$$

In the Regime-I with $h < h_c$, detwinning in both Cu and HEA is suppressed after He-implantation, and thus the irradiation hardening can be calculated by

$$\Delta H_{\text{irradiation}} = \Delta H_{\text{twin}} + \Delta H_{\text{bubble}} = (\xi_{\text{Cu}} \Delta H_{\text{twin}}^{\text{Cu}} + \xi_{\text{HEA}} \Delta H_{\text{twin}}^{\text{HEA}}) + (\xi_{\text{Cu}} \Delta H_{\text{bubble}}^{\text{Cu}} + \xi_{\text{HEA}} \Delta H_{\text{bubble}}^{\text{HEA}}), \quad (10\text{a})$$

While in the Regime-II with $h \geq h_c$, detwinning in Cu is suppressed, and the stability nanotwins in HEA seems not to be influenced by He defects. Thus, the irradiation hardening can be calculated by

$$\Delta H_{\text{irradiation}} = \Delta H_{\text{twin}} + \Delta H_{\text{bubble}} = \xi_{\text{Cu}} \Delta H_{\text{twin}}^{\text{Cu}} + (\xi_{\text{Cu}} \Delta H_{\text{bubble}}^{\text{Cu}} + \xi_{\text{HEA}} \Delta H_{\text{bubble}}^{\text{HEA}}). \quad (10\text{b})$$

For the sake of simplicity, assuming $\tau_i = 0.07$ GPa, the modified CLS model captures the experimental data of the He-irradiated NMMs well, see the dash line in Fig. 10(d). For comparison, the average shear strength of bubbles (τ_i) for V/Ag and Cu/V multi-layers is 0.052 and 0.064 GPa (Wei et al., 2011), respectively, close to our finding of $\tau_i \sim 0.07$ GPa. Our results suggested that He bubbles make a significant contribution to the strength, particularly at $h \geq 50$ nm.

4.4. Size-dependent strain rate sensitivity of Cu/HEA NLs

4.4.1. As-deposited HEA/Cu NTNLs

Prior results (Chen et al., 2006; Cheng et al., 2005; Khan and Liu, 2016) uncovered that the SRS m of FCC metals generally increases with reducing grain sizes d , which can be further enhanced by introducing nanotwins into the matrix. The rate dependence of the flow stress is normally attributed to the thermally activated process of overcoming the obstacles to dislocation motion. Therefore, the SRS m related to the activation volume V^* in a thermally activated event can be given by (Bouaziz, 2012; Cheng et al., 2005; Khan et al., 2015):

$$m = \frac{\sqrt{3}k_B T}{\sigma V^*} = \frac{\sqrt{3}k_B T}{\sigma b_p \lambda l^*}. \quad (11)$$

Assume the evolution of the effective dislocation segment length l^* is controlled by the geometrical length of microstructure L , one gets $l^* = \psi \cdot L$, where ψ is a coefficient. Based on this theory, we discuss the underlying mechanisms of the size-dependent SRS for the un-irradiated Cu/HEA NTNLs as follows.

In the regime-II with $h > h_c$, contrary to the general belief that the SRS m of FCC metals increases as the characteristic size decreases, the present FCC/FCC HEA/Cu NTNLs exhibit the reduced SRS m as a whole. Given HEA and Cu co-deform, following the derivation by Fan et al. (2017), which involves the interface effect on the rate-limiting process, the SRS m of HEA/Cu NTNLs can be expressed as:

$$m = \xi_{\text{Cu}} \cdot m_{\text{Cu}} + \xi_{\text{HEA}} \cdot m_{\text{HEA}}, \quad (12)$$

where m_{Cu} and m_{HEA} are the SRS of Cu and HEA constituents, respectively. In the HEA/Cu NTNLs, the effective size h^* and twin thickness λ are the main microstructural limitation for gliding dislocations, thus the effective dislocation segment length l^* can be expressed as: $\frac{1}{l^*} = \frac{1}{\psi L} = \frac{1}{\psi h^*} + \frac{P^T}{\psi \lambda}$. Correspondingly, the SRS m of Cu and HEA in HEA/Cu NTNLs can be respectively given by:

$$m_{\text{Cu}} = \frac{\sqrt{3}k_B T}{\sigma_{\text{Cu}} b_{p,\text{Cu}}^2} \left(\frac{1}{\psi h_{\text{Cu}}^*} + \frac{P^T}{\psi \lambda_{\text{Cu}}} \right), \quad (13\text{a})$$

$$m_{\text{HEA}} = \frac{\sqrt{3}k_B T}{\sigma_{\text{HEA}} b_{p,\text{HEA}}^2} \left(\frac{1}{\psi h_{\text{HEA}}^*} + \frac{1}{\psi \lambda_{\text{HEA}}} \right), \quad (13\text{b})$$

where the symbols have the same meaning as before, and the subscripts represent the constituent of Cu and HEA, respectively. Taking the parameter of $\psi = 3.45$, this model broadly captures the trend of SRS m at large $h > h_c$, as shown in Fig. 12(c).

By contrast, in the regime-I with $h \leq h_c$, Eq. (13) far overestimates the experimental data and is inappropriate to explaining the trend of SRS m . In fact, this variation trend of SRS m may be related to the interfacial structure. In the regime-I, the interface becomes fully coherent in a single crystal-like columnar grain, so that the length of dislocation segment is confined by the dislocation density rather than the interface (Liu et al., 2019). In this case, it is the dislocation density ρ rather than the twin thickness λ that determines the SRS m of HEA/Cu NTNLs. In our work, λ remains approximately at the same level (~5 nm) and is almost independence on h . Specifically, plastic deformation facilitates the detwinning behavior via slip of detwinning partials along the TB. Here, the effective dislocation segment length l^* is on the order of 5 nm estimated from the initial dislocation density ρ (close to λ). Thus, following the treatment of Liu et al. (2019), we only consider the effect of the initial dislocation density on SRS m of HEA/Cu NTNLs in this regime, and the nanotwin effect is neglected. Accordingly, the effective length l^* can be given by: $l^* = \frac{a}{\sqrt{\rho}}$ (Liu et al., 2019; Wei, 2007), and thus SRS m can be written as:

$$m_{\text{Cu}} = \frac{\sqrt{3}k_B T}{\sigma_{\text{Cu}} b_{p,\text{Cu}}^2} \frac{1}{a/\sqrt{\rho}}, \quad (14\text{a})$$

$$m_{HEA} = \frac{\sqrt{3}k_B T}{\sigma_{HEA} b_{p,HEA}^2} \frac{1}{a/\sqrt{\rho}}, \quad (14b)$$

where ρ is the initial dislocation density, a is retained as proportionality factors, other symbols have the same meaning as mentioned above. Taking $\rho = 5 \times 10^{12} \text{ cm}^{-2}$ and $a = 1.2 \times 10^7$, it appears that the calculation result agrees well with experimental data at small $h \leq h_c$, see Fig. 12(c).

4.4.2. Irradiated HEA/Cu NTNLs

The difference in the size-dependent SRS m between as-deposited and irradiated HEA/Cu NTNLs suggests that the irradiation-induced He defects can strongly alter the mechanical response of HEA/Cu NTNLs. In particular, the positive-to-negative transition of SRS m with decreasing h in irradiated HEA/Cu NTNLs may be mainly attributed to the h -dependent content of He bubbles as well as He atoms/clusters. A possible explanation is as follows.

Based on previous work (Soare and Curtin, 2008; Wu et al., 2018a,b), we qualitatively explain that the negative SRS m caused by irradiation can be attributed to the dynamic strain aging (DSA). DSA is usually associated with an increase in the strength of an alloy due to the diffusion of solutes around dislocations that temporarily hinder dislocation motion, rendering the negative SRS m (Soare and Curtin, 2008). Similarly, the He bubbles in constituent layers as weak obstacles to dislocation slip would trigger the dynamic strain aging (DSA) effect that induces the negative SRS m . This is because these bubbles tend to coarsen with time and, especially, the coarsening process is accelerated with the deformation process. During plastic deformation, in addition to the lattice diffusion of He atoms, the formation of larger sized He bubbles with greater strength can be achieved through bubble migration and coalescence. Obviously, the time-dependent process indicates that larger He bubbles can hinder dislocation motion more effectively. At smaller strain rates, these He atoms/clusters have enough time to migrate and form larger average sized bubbles. The average intensity of He bubbles increases as the strain rate decreases (Wu et al., 2018a,b). Therefore, the dynamic bubble strengthening mechanism induces the negative SRS.

At the same time, a recent study (Hooshmand and Ghazisaeidi, 2020) has shown that the presence of solutes will affect the energetics of twin growth. At low strain rates, twin growth is slow and the TB will be subjected to additional pinning stresses imposed by the separated solutes. If the applied stress is lower than this value, the boundary will still be captured and the twin growth will be suppressed. Solute strengthening due to the suppression of twin growth caused by solute separation can lead to DSA and negative SRS. Similarly, in irradiated HEA/Cu NTNLs, He atoms/clusters will migrate to TBs during deformation, making them difficult to accommodate external plastic strains (by detwinning, i.e., the reverse process of twinning) via pinning TBs. Obviously, this migration/diffusion process of He defects is time-dependent. At lower strain rates, more He defects have enough time to pin TBs, resulting in a more pronounced hardening effect. Therefore, the interaction of He atoms/clusters and TBs can lead to DSA and negative SRS as well.

Taken together, the dislocation-bubble interactions and those of twin boundary-He atoms/clusters both contribute to the negative SRS m . Specifically, in this study a higher density of He defects leads to a smaller value of SRS m , analogous to that of binary Cu-based alloyed thin films (e.g. Cu-Cr, Cu-Mo) (Zhang et al., 2014a, 2018a). On the other hand, the layer interfaces in general enhance SRS m , accompanied with the trend that a higher interface density results in large positive SRS m . Although the fully coherent interfaces formed at small h induce the reduction in SRS m (Liu et al., 2019), these nanotwins stabilized by He defects in irradiated constituent layers can further enhance SRS m of irradiated NLs. Therefore, the competing effect between the dislocation-coherent interface/boundary interaction (that induces increased positive SRS) and the combination of dislocation-bubble and twin boundary-He atoms/clusters interactions (that induces reduced negative SRS) probably renders the transition from positive to negative SRS m with decreasing h .

5. Conclusion

In this work, we investigated the microstructural stability and mechanical properties of HEA/Cu NTNLs before and after He-ion irradiation. The main findings provide new insights into designing the nanolaminates containing HEAs with desirable mechanical properties, which are summarized as follows.

- (1) The confined nanotwins in Cu and penetrated nanotwins are preferred to detwin during plastic deformation, while the He defects can suppress detwinning of nanotwins via pinning the migration of twin boundaries.
- (2) Both as-deposited and irradiated HEA/Cu NTNLs manifest the trend of “smaller is stronger”. The He-implantation remarkably enhances the hardness of as-deposited HEA/Cu NTNLs, associated with the minimum irradiation hardening at $h \sim 10 \text{ nm}$.
- (3) The as-deposited HEA/Cu NTNLs exhibit the monotonically reduced SRS m with reducing h owing to the increased propensity of detwinning. While the irradiated HEA/Cu NTNLs manifest the transition from the positive to the negative SRS m , owing to the competing effects between the dislocation-coherent interface/boundary interactions (that induces increased positive SRS) and the combination of dislocation-bubble and TB-He atoms/clusters interactions (that induces reduced negative SRS).

Credit author contribution statement

H.H. Chen: I have made substantial contributions to the conception or design of the work; or the acquisition, analysis, or interpretation of data for the work; AND I have drafted the work or revised it critically for important intellectual content; AND I have

approved the final version to be published; AND I agree to be accountable for all aspects of the work in ensuring that questions related to the accuracy or integrity of any part of the work are appropriately investigated and resolved, All persons who have made substantial contributions to the work reported in the manuscript, including those who provided editing and writing assistance but who are not authors, are named in the Acknowledgments section of the manuscript and have given their written permission to be named. **Y.F. Zhao:** All persons who have made substantial contributions to the work reported in the manuscript, including those who provided editing and writing assistance but who are not authors, are named in the Acknowledgments section of the manuscript and have given their written permission to be named. **J.Y. Zhang:** All persons who have made substantial contributions to the work reported in the manuscript, including those who provided editing and writing assistance but who are not authors, are named in the Acknowledgments section of the manuscript and have given their written permission to be named. **Y.Q. Wang:** All persons who have made substantial contributions to the work reported in the manuscript, including those who provided editing and writing assistance but who are not authors, are named in the Acknowledgments section of the manuscript and have given their written permission to be named. **G.Y. Li:** All persons who have made substantial contributions to the work reported in the manuscript, including those who provided editing and writing assistance but who are not authors, are named in the Acknowledgments section of the manuscript and have given their written permission to be named. **K. Wu:** All persons who have made substantial contributions to the work reported in the manuscript, including those who provided editing and writing assistance but who are not authors, are named in the Acknowledgments section of the manuscript and have given their written permission to be named. **G. Liu:** All persons who have made substantial contributions to the work reported in the manuscript, including those who provided editing and writing assistance but who are not authors, are named in the Acknowledgments section of the manuscript and have given their written permission to be named. **J. Sun:** All persons who have made substantial contributions to the work reported in the manuscript, including those who provided editing and writing assistance but who are not authors, are named in the Acknowledgments section of the manuscript and have given their written permission to be named.

Declaration of competing interest

The authors declare that they have no known competing financial interests or personal relationships that could have appeared to influence the work reported in this paper.

Acknowledgements

This work was supported by the National Natural Science Foundation of China (Grant Nos. 51722104, 51625103, 51790482, and 51761135031), the National Key Research and Development Program of China (2017YFA0700701) and the 111 Project 2.0 of China (BP2018008). This work is also supported by the International Joint Laboratory for Micro/Nano Manufacturing and Measurement Technologies. JYZ is grateful for the Fok Ying-Tong Education Foundation (161096) and the Fundamental Research Funds for the Central Universities for part of financial support. We thank Dr. S.W. Guo of XJTU and Dr. J. Li at the Instrument Analysis Center of XJTU for their great assistance of TEM analysis.

References

- Anderson, P.M., Foecke, T., Bulletin, P.M.H.J.M., 1999. Dislocation-based deformation mechanisms in metallic nanolaminates. *MRS Bull.* 24, 27–33.
- Anderoglu, O., Misra, A., Wang, J., Hoagland, R.G., Hirth, J.P., Zhang, X., 2010. Plastic flow stability of nanotwinned Cu foils. *Int. J. Plast.* 26, 875–886.
- Asaro, R.J., Suresh, S., 2005. Mechanistic models for the activation volume and rate sensitivity in metals with nanocrystalline grains and nano-scale twins. *Acta Mater.* 53, 3369–3382.
- Beyerlein, I.J., Demkowicz, M.J., Misra, A., Uberuaga, B.P., 2015. Defect-interface interactions. *Prog. Mater. Sci.* 74, 125–210.
- Beyerlein, I.J., Wang, J., 2019. Interface-driven mechanisms in cubic/noncubic nanolaminates at different scales. *MRS Bull.* 44, 31–39.
- Bhattacharya, D., Mara, N.A., Dickerson, P., Hoagland, R.G., Misra, A., 2011. Transmission electron microscopy study of the deformation behavior of Cu/Nb and Cu/Ni nanoscale multilayers during nanoindentation. *J. Mater. Res.* 24, 1291–1302.
- Bouaziz, O., 2012. Strain-hardening of twinning-induced plasticity steels. *Scripta Mater.* 66, 982–985.
- Cantor, B., Chang, I.T.H., Knight, P., Vincent, A.J.B., 2004. Microstructural development in equiatomic multicomponent alloys. *Mater. Sci. Eng., A* 375, 213–218.
- Cao, Z.H., Cai, Y., Sun, C., Ma, Y.J., Wei, M.Z., Li, Q., Lu, H.M., Wang, H., Zhang, X.K., 2019. Tailoring strength and plasticity of Ag/Nb nanolaminates via intrinsic microstructure and extrinsic dimension. *Int. J. Plast.* 113, 145–157.
- Cao, Z.H., Sun, W., Yang, X.B., Zhao, J.W., Ma, Y.J., Meng, X.K., 2018. Intersectant coherent twin boundaries governed strong strain hardening behavior in nanocrystalline Cu. *Int. J. Plast.* 103, 81–94.
- Cao, Z.H., Wei, M.Z., Ma, Y.J., Sun, C., Lu, H.M., Fan, Z., Meng, X.K., 2017. Cyclic deformation induced strengthening and unusual rate sensitivity in Cu/Ru nanolayered films. *Int. J. Plast.* 99, 43–57.
- Chen, D., Wang, J., Chen, T., Shao, L., 2013. Defect annihilation at grain boundaries in alpha-Fe. *Sci. Rep.* 3, 1450.
- Chen, J., Lu, L., Lu, K., 2006. Hardness and strain rate sensitivity of nanocrystalline Cu. *Scripta Mater.* 54, 1913–1918.
- Chen, Y., Liu, Y., Fu, E.G., Sun, C., Yu, K.Y., Song, M., Li, J., Wang, Y.Q., Wang, H., Zhang, X., 2015. Unusual size-dependent strengthening mechanisms in helium ion-irradiated immiscible coherent Cu/Co nanolayers. *Acta Mater.* 84, 393–404.
- Chen, Y., Liu, Y., Sun, C., Yu, K.Y., Song, M., Wang, H., Zhang, X., 2012. Microstructure and strengthening mechanisms in Cu/Fe multilayers. *Acta Mater.* 60, 6312–6321.
- Cheng, S., Ma, E., Wang, Y.M., Kecskes, L.J., Youssef, K.M., Koch, C.C., Trociewitz, U.P., Han, K., 2005. Tensile properties of in situ consolidated nanocrystalline Cu. *Acta Mater.* 53, 1521–1533.
- Colla, M.S., Wang, B., Idrissi, H., Schryvers, D., Raskin, J.P., Pardo, T., 2012. High strength-ductility of thin nanocrystalline palladium films with nanoscale twins: on-chip testing and grain aggregate model. *Acta Mater.* 60, 1795–1806.
- Dalla Torre, F., Späth, P., Schäublin, R., Victoria, M., 2005. Deformation behaviour and microstructure of nanocrystalline electrodeposited and high pressure torsion nickel. *Acta Mater.* 53, 2337–2349.
- Demkowicz, M.J., Hoagland, R.G., Hirth, J.P., 2008. Interface structure and radiation damage resistance in Cu-Nb multilayer nanocomposites. *Phys. Rev. Lett.* 100, 136102.

- Ding, Z.Y., He, Q.F., Wang, Q., Yang, Y., 2018. Superb strength and high plasticity in laves phase rich eutectic medium-entropy-alloy nanocomposites. *Int. J. Plast.* 106, 57–72.
- Fan, C., Li, Q., Ding, J., Liang, Y., Shang, Z., Li, J., Su, R., Cho, J., Chen, D., Wang, Y., Wang, J., Wang, H., Zhang, X., 2019a. Helium irradiation induced ultra-high strength nanotwinned Cu with nanovoids. *Acta Mater.* 177, 107–120.
- Fan, J.T., Zhang, L.J., Yu, P.F., Zhang, M.D., Li, G., Liaw, P.K., Liu, R.P., 2019b. A novel high-entropy alloy with a dendrite-composite microstructure and remarkable compression performance. *Scripta Mater.* 159, 18–23.
- Fan, Z., Liu, Y., Xue, S., Rahimi, R.M., Bahr, D.F., Wang, H., Zhang, X., 2017. Layer thickness dependent strain rate sensitivity of Cu/amorphous CuNb multilayer. *Appl. Phys. Lett.* 110, 161905.
- Fan, Z., Zhao, S., Jin, K., Chen, D., Osetskiy, Y.N., Wang, Y., Bei, H., More, K.L., Zhang, Y., 2019c. Helium irradiated cavity formation and defect energetics in Ni-based binary single-phase concentrated solid solution alloys. *Acta Mater.* 164, 283–292.
- Fang, Q., Chen, Y., Li, J., Jiang, C., Liu, B., Liu, Y., Liaw, P.K., 2019. Probing the phase transformation and dislocation evolution in dual-phase high-entropy alloys. *Int. J. Plast.* 114, 161–173.
- Feng, H., Tang, J.W., Chen, H.T., Tian, Y.Y., Fang, Q.H., Li, J., Liu, F., 2020. Indentation-induced plastic behaviour of nanotwinned Cu/high entropy alloy FeCoCrNi nanolaminates: an atomic simulation. *RSC Adv.* 10, 9187–9192.
- Feng, X.B., Fu, W., Zhang, J.Y., Zhao, J.T., Li, J., Wu, K., Liu, G., Sun, J., 2017. Effects of nanotwins on the mechanical properties of AlxCoCrFeNi high entropy alloy thin films. *Scripta Mater.* 139, 71–76.
- Frutos, E., Callisti, M., Karlik, M., Polcar, T., 2015. Length-scale-dependent mechanical behaviour of Zr/Nb multilayers as a function of individual layer thickness. *Mater. Sci. Eng.* 632, 137–146.
- Fu, E.G., Misra, A., Wang, H., Shao, L., Zhang, X., 2010. Interface enabled defects reduction in helium ion irradiated Cu/V nanolayers. *J. Nucl. Mater.* 407, 178–188.
- Fu, Z., Chen, W., Wen, H., Zhang, D., Chen, Z., Zheng, B., Zhou, Y., Lavernia, E.J., 2016. Microstructure and strengthening mechanisms in an FCC structured single-phase nanocrystalline Co 25 Ni 25 Fe 25 Al 7.5 Cu 17.5 high-entropy alloy. *Acta Mater.* 107, 59–71.
- Ganji, R.S., Sai Karthik, P., Bhanu Sankara Rao, K., Rajulapati, K.V., 2017. Strengthening mechanisms in equiatomic ultrafine grained AlCoCrCuFeNi high-entropy alloy studied by micro- and nanoindentation methods. *Acta Mater.* 125, 58–68.
- George, E.P., Raabe, D., Ritchie, R.O., 2019. High-entropy alloys. *Nat. Rev. Mater.* 4, 515–534.
- Gludovatz, B., Hohenwarter, A., Cattoor, D., Chang, E.H., George, E.P., Ritchie, R.O., 2014. A fracture-resistant high-entropy alloy for cryogenic applications. *Science* 345, 1153–1158.
- Han, W., Fu, E.G., Demkowicz, M.J., Wang, Y., Misra, A., 2013. Irradiation damage of single crystal, coarse-grained, and nanograined copper under helium bombardment at 450 °C. *J. Mater. Res.* 28, 2763–2770.
- Hansen, B.L., Carpenter, J.S., Sintay, S.D., Bronkhorst, C.A., McCabe, R.J., Mayeur, J.R., Mourad, H.M., Beyerlein, I.J., Mara, N.A., Chen, S.R., Gray, G.T., 2013. Modeling the texture evolution of Cu/Nb layered composites during rolling. *Int. J. Plast.* 49, 71–84.
- Hasana, M.N., Ana, X.H., Gue, J., Song, M., Cao, Y., Li, Y.S., Zhub, Y.T., 2019. Simultaneously enhancing strength and ductility of a high-entropy alloy via gradient hierarchical microstructures. *Int. J. Plast.* 123, 178–195.
- He, J.Y., Liu, W.H., Wang, H., Wu, Y., Liu, X.J., Nieh, T.G., Lu, Z.P., 2014. Effects of Al addition on structural evolution and tensile properties of the FeCoNiCrMn high-entropy alloy system. *Acta Mater.* 62, 105–113.
- Hooshmand, M.S., Ghazisaeidi, M., 2020. Solute/twin boundary interaction as a new atomic-scale mechanism for dynamic strain aging. *Acta Mater.* 188, 711–719.
- Jawaharam, G.S., Barr, C.M., Monterrosa, A.M., Hattar, K., Averback, R.S., Dillon, S.J., 2020. Irradiation induced creep in nanocrystalline high entropy alloys. *Acta Mater.* 182, 68–76.
- Jiang, S.Y., Sun, D., Zhang, Y.Q., Wang, S.B., Zhao, C.Z., 2017. Plastic deformation mechanisms of equiatomic Ni₂₀Ti₂₀Fe₂₀Al₂₀Cu₂₀ high-entropy alloy at high temperatures. *J. Mater. Sci.* 52, 3199–3207.
- Juan, C.C., Tsai, M.H., Tsai, C.W., Lin, C.M., Wang, W.R., Yang, C.C., Chen, S.K., Lin, S.J., Yeh, J.W., 2015. Enhanced mechanical properties of HfMoTaTiZr and HfMoNbTaTiZr refractory high-entropy alloys. *Intermetallics* 62, 76–83.
- Kaoumi, D., Motta, A.T., Birtcher, R.C., 2008. A thermal spike model of grain growth under irradiation. *J. Appl. Phys.* 104.
- Kashinath, A., Misra, A., Demkowicz, M.J., 2013. Stable storage of helium in nanoscale platelets at semicoherent interfaces. *Phys. Rev. Lett.* 110, 086101.
- Khan, A.S., Liu, J., 2016. A deformation mechanism based crystal plasticity model of ultrafine-grained/nanocrystalline FCC polycrystals. *Int. J. Plast.* 86, 56–69.
- Khan, A.S., Liu, J., Yoon, J.W., Nambori, R., 2015. Strain rate effect of high purity aluminum single crystals: experiments and simulations. *Int. J. Plast.* 67, 39–52.
- Koehler, J.S., 1970. Attempt to design a strong solid. *Phys. Rev. B* 2, 547–551.
- Li, D., Li, C., Feng, T., Zhang, Y., Sha, G., Lewandowski, J.J., Liaw, P.K., Zhang, Y., 2017a. High-entropy Al_{0.3}CoCrFeNi alloy fibers with high tensile strength and ductility at ambient and cryogenic temperatures. *Acta Mater.* 123, 285–294.
- Li, J., Chen, Y., Xue, S., Wang, H., Zhang, X., 2016a. Comparison of size dependent strengthening mechanisms in Ag/Fe and Ag/Ni multilayers. *Acta Mater.* 114, 154–163.
- Li, J., Yu, K.Y., Chen, Y., Song, M., Wang, H., Kirk, M.A., Li, M., Zhang, X., 2015. In situ study of defect migration kinetics and self-healing of twin boundaries in heavy ion irradiated nanotwinned metals. *Nano Lett.* 15, 2922–2927.
- Li, J., Zhang, J.Y., Liu, G., Sun, J., 2016b. New insight into the stable grain size of nanotwinned Ni in steady-state creep: effect of the ratio of effective-to-internal stress. *Int. J. Plast.* 85, 172–189.
- Li, N., Fu, E.G., Wang, H., Carter, J.J., Shao, L., Maloy, S.A., Misra, A., Zhang, X., 2009. He ion irradiation damage in Fe/W nanolayer films. *J. Nucl. Mater.* 389, 233–238.
- Li, N., Nastasi, M., Misra, A., 2012. Defect structures and hardening mechanisms in high dose helium ion implanted Cu and Cu/Nb multilayer thin films. *Int. J. Plast.* 32–33, 1–16.
- Li, N., Wang, J., Misra, A., Zhang, X., Huang, J.Y., Hirth, J.P., 2011. Twinning dislocation multiplication at a coherent twin boundary. *Acta Mater.* 59, 5989–5996.
- Li, X., Kreuter, T., Luo, X.M., Schwaiger, R., Zhang, G.P., 2017b. Detecting co-deformation behavior of Cu–Au nanolayered composites. *Mater. Res. Lett.* 5, 20–28.
- Li, X., Wei, Y., Lu, L., Lu, K., Gao, H., 2010. Dislocation nucleation governed softening and maximum strength in nano-twinned metals. *Nature* 464, 877.
- Liang, F., Zhang, B., Yong, Y., Luo, X.M., Zhang, G.P., 2020. Enhanced strain delocalization through formation of dispersive micro shear bands in laminated Ni. *Int. J. Plast.* <https://doi.org/10.1016/j.ijplas.2020.102745>.
- Liang, X.Q., Wang, Y.Q., Zhao, J.T., Wu, S.H., Wu, K., Liu, G., Sun, J., 2019. Size- and ion-dose-dependent microstructural evolution and hardening in He-irradiated miscible Cu/Zr crystalline/crystalline nanolaminates. *Surf. Coatings. Technol.* 366, 255–265.
- Liu, Y., Bufford, D., Wang, H., Sun, C., Zhang, Y., 2011. Mechanical properties of highly textured Cu/Ni multilayers. *Acta Mater.* 59, 1924–1933.
- Liu, Y., Chen, Y., Yu, K.Y., Wang, H., Chen, J., Zhang, X., 2013. Stacking fault and partial dislocation dominated strengthening mechanisms in highly textured Cu/Co multilayers. *Int. J. Plast.* 49, 152–163.
- Liu, Y., Yang, K.M., Hay, J., Fu, E.G., Zhang, X., 2019. The effect of coherent interface on strain-rate sensitivity of highly textured Cu/Ni and Cu/V multilayers. *Scripta Mater.* 162, 33–37.
- Lu, C., Niu, L., Chen, N., Jin, K., Yang, T., Xiu, P., Zhang, Y., Gao, F., Bei, H., Shi, S., He, M.R., Robertson, I.M., Weber, W.J., Wang, L., 2016. Enhancing radiation tolerance by controlling defect mobility and migration pathways in multicomponent single-phase alloys. *Nat. Commun.* 7, 13564.
- Lu, C., Yang, T., Jin, K., Gao, N., Xiu, P., Zhang, Y., Gao, F., Bei, H., Weber, W.J., Sun, K., Dong, Y., Wang, L., 2017a. Radiation-induced segregation on defect clusters in single-phase concentrated solid-solution alloys. *Acta Mater.* 127, 98–107.
- Lu, K., Lu, L., Suresh, S., 2009. Strengthening materials by engineering coherent internal boundaries at the nanoscale. *Science* 324, 349–352.
- Lu, Y., Gao, X., Jiang, L., Chen, Z., Wang, T., Jie, J., Kang, H., Zhang, Y., Guo, S., Ruan, H., Zhao, Y., Cao, Z., Li, T., 2017b. Directly cast bulk eutectic and near-eutectic high entropy alloys with balanced strength and ductility in a wide temperature range. *Acta Mater.* 124, 143–150.
- MacDonald, B.E., Fu, Z., Wang, X., Li, Z., Chen, W., Zhou, Y., Raabe, D., Schoenung, J., Hahn, H., Lavernia, E.J., 2019. Influence of phase decomposition on mechanical behavior of an equiatomic CoCuFeMnNi high entropy alloy. *Acta Mater.* 181, 25–35.

- Misra, A., Hirth, J.P., Hoagland, R.G., 2005. Length-scale-dependent deformation mechanisms in incoherent metallic multilayered composites. *Acta Mater.* 53, 4817–4824.
- Misra, A., Verdier, M., Lu, Y.C., Kung, H., Mitchell, T.E., Nastasi, M., Embury, J.D., 1998. Structure and mechanical properties of Cu-X (X = Nb,Cr,Ni) nanolayered composites. *Scripta Mater.* 39, 555–560.
- Niu, J.J., Zhang, J.Y., Liu, G., Zhang, P., Lei, S.Y., Zhang, G.J., Sun, J., 2012. Size-dependent deformation mechanisms and strain-rate sensitivity in nanostructured Cu/X (X=Cr, Zr) multilayer films. *Acta Mater.* 60, 3677–3689.
- Ritchie, R.O., 2011. The conflicts between strength and toughness. *Nat. Mater.* 10, 817.
- Schuh, B., Mendez-Martin, F., Völker, B., George, E.P., Clemens, H., Pippan, R., Hohenwarter, A., 2015. Mechanical properties, microstructure and thermal stability of a nanocrystalline CoCrFeMnNi high-entropy alloy after severe plastic deformation. *Acta Mater.* 96, 258–268.
- Shen, Y.F., Lu, L., Dao, M., Suresh, S., 2006. Strain rate sensitivity of Cu with nanoscale twins. *Scripta Mater.* 55, 319–322.
- Soare, M.A., Curtin, W.A., 2008. Single-mechanism rate theory for dynamic strain aging in fcc metals. *Acta Mater.* 56, 4091–4101.
- Stoller, R.E., Toloczko, M.B., Was, G.S., Certain, A.G., Dwaraknath, S., Garner, F.A., 2013. On the use of SRIM for computing radiation damage exposure. *Nucl. Instrum. Methods Phys. Res., Sect. B* 310, 75–80.
- Tang, Z., Yuan, T., Tsai, C.W., Yeh, J.W., Lundin, C.D., Liaw, P.K., 2015. Fatigue behavior of a wrought Al0.5CoCrCuFeNi two-phase high-entropy alloy. *Acta Mater.* 99, 247–258.
- Tsai, M.H., Yeh, J.W., Gan, J.Y., 2008. Diffusion barrier properties of AlMoNbSiTaTiVZr high-entropy alloy layer between copper and silicon. *Thin Solid Films* 516, 5527–5530.
- Varvenne, C., Leyson, G.P.M., Ghazisaeidic, M., Curtin, W.A., 2017. Solute strengthening in random alloys. *Acta Mater.* 124, 660–683.
- Varvenne, C., Luque, A., Curtin, W.A., 2016. Theory of strengthening in fcc high entropy alloys. *Acta Mater.* 118, 164–176.
- Wang, J., Li, N., Anderoglu, O., Zhang, X., Misra, A., Huang, J.Y., Hirth, J.P., 2010. Detwinning mechanisms for growth twins in face-centered cubic metals. *Acta Mater.* 58, 2262–2270.
- Wang, M., Beyerlein, I.J., Zhang, J., Han, W.-Z., 2018. Defect-interface interactions in irradiated Cu/Ag nanocomposites. *Acta Mater.* 160, 211–223.
- Wang, W.R., Wang, W.L., Wang, S.C., Tsai, Y.C., Lai, C.H., Yeh, J.W., 2012. Effects of Al addition on the microstructure and mechanical property of AlxCoCrFeNi high-entropy alloys. *Intermetallics* 26, 44–51.
- Wang, Y.M., Hamza, A.V., Ma, E., 2006. Temperature-dependent strain rate sensitivity and activation volume of nanocrystalline Ni. *Acta Mater.* 54, 2715–2726.
- Wang, Z., Wang, C., Zhao, Y.L., 2020. High hardness and fatigue resistance of CoCrFeMnNi high entropy alloy films with ultrahigh-density nanotwins. *Int. J. Plast.* <https://doi.org/10.1016/j.ijplas.2020.102726>.
- Wei, Q., 2007. Strain rate effects in the ultrafine grain and nanocrystalline regimes—Influence on some constitutive responses. *J. Mater. Sci.* 42, 1709–1727.
- Wei, Q.M., Li, N., Mara, N., Nastasi, M., Misra, A., 2011. Suppression of irradiation hardening in nanoscale V/Ag multilayers. *Acta Mater.* 59, 6331–6340.
- Wei, S., Zhang, L., Zheng, S., Wang, X., Wang, J., 2019. Deformation-induced interfacial transition zone in Cu/V nanolamellar multilayers. *Scripta Mater.* 159, 104–108.
- Wu, S.H., Cheng, P.M., Wu, K., Hou, Z.Q., Wang, Y.Q., Liang, X.Q., Li, J., Kuang, J., Zhang, J.Y., Liu, G., Sun, J., 2018a. Effect of He-irradiation fluence on the size-dependent hardening and deformation of nanostructured Mo/Zr multilayers. *Int. J. Plast.* 111, 36–52.
- Wu, Y., Bonisch, M., Alkan, S., Abuzaid, W., Sehitoglu, H., 2018b. Experimental determination of latent hardening coefficients in FeMnNiCoCr. *Int. J. Plast.* 105, 239–260.
- Yan, J.W., Zhu, X.F., Yang, B., Zhang, G.P., 2013. Shear stress-driven refreshing capability of plastic deformation in nanolayered metals. *Phys. Rev. Lett.* 110, 155502.
- Yang, T.N., Lu, C., Jin, K., Crespillo, M.L., Zhang, Y., Bei, H., Wang, L., 2017. The effect of injected interstitials on void formation in self-ion irradiated nickel containing concentrated solid solution alloys. *J. Nucl. Mater.* 488, 328–337.
- Yeh, J.W., Chen, S.K., Lin, S.J., Gan, J.Y., Chin, T.S., Shun, T.T., Tsau, C.H., Chang, S.Y., 2004. Nanostructured high-entropy alloys with multiple principal elements: novel alloy design concepts and outcomes. *Adv. Eng. Mater.* 6, 299–303.
- Yu, K.Y., Bufford, D., Khatkhatay, F., Wang, H., Kirk, M.A., Zhang, X., 2013a. In situ studies of irradiation-induced twin boundary migration in nanotwinned Ag. *Scripta Mater.* 69, 385–388.
- Yu, K.Y., Liu, Y., Fu, E.G., Wang, Y.Q., Myers, M.T., Wang, H., Shao, L., Zhang, X., 2013b. Comparisons of radiation damage in He ion and proton irradiated immiscible Ag/Ni nanolayers. *J. Nucl. Mater.* 440, 310–318.
- Zhang, H., Ren, F., Wang, Y., Hong, M., Xiao, X., Qin, W., Jiang, C., 2015a. In situ TEM observation of helium bubble evolution in V/Ag multilayer during annealing. *J. Nucl. Mater.* 467, 537–543.
- Zhang, J.Y., Wang, Y.Q., Liang, X.Q., Zeng, F.L., Liu, G., Sun, J., 2015b. Size-dependent He-irradiated tolerance and plastic deformation of crystalline/amorphous Cu/Cu-Zr nanolaminates. *Acta Mater.* 92, 140–151.
- Zhang, J.Y., Wang, Y.Q., Wu, K., Zhang, P., Liu, G., Zhang, G.J., Sun, J.J.M.S., A, E., 2014a. Strain rate sensitivity of nanolayered Cu/X (X=Cr, Zr) micropillars: effects of heterophase interface/twin boundary. *Mater. Sci. Eng.* 612, 28–40.
- Zhang, J.Y., Wu, K., Zhang, L.Y., Wang, Y.Q., Liu, G., Sun, J., 2017. Unraveling the correlation between Hall-Petch slope and peak hardness in metallic nanolaminates. *Int. J. Plast.* 96, 120–134.
- Zhang, J.Y., Zeng, F.L., Wu, K., Wang, Y.Q., Liang, X.Q., Liu, G., Zhang, G.J., Sun, J., 2016. Size-dependent plastic deformation characteristics in He-irradiated nanostructured Cu/Mo multilayers: competition between dislocation-boundary and dislocation-bubble interactions. *Mater. Sci. Eng.* 673, 530–540.
- Zhang, J.Y., Zhao, J.T., Li, X.G., Wang, Y.Q., Wu, K., Liu, G., Sun, J., 2018a. Alloying effects on the microstructure and mechanical properties of nanocrystalline Cu-based alloyed thin films: miscible Cu-Ti vs immiscible Cu-Mo. *Acta Mater.* 143, 55–66.
- Zhang, T.W.M.S.G., Zhao, D., Wu, Y.C., Zhang, Y., Wang, Z.H., Qiao, J.W., 2020. Simultaneous enhancement of strength and ductility in a NiCoCrFe high-entropy alloy upon dynamic tension: micromechanism and constitutive modeling. *Int. J. Plast.* 124, 226–246.
- Zhang, W., Wang, M., Wang, L., Liu, C.H., Chang, H., Yang, J.J., Liao, J.L., Yang, Y.Y., Liu, N., 2019. Interface stability, mechanical and corrosion properties of AlCrMoNbZr/(AlCrMoNbZr)N high-entropy alloy multilayer coatings under helium ion irradiation. *Appl. Surf. Sci.* 485, 108–118.
- Zhang, X., Hattar, K., Chen, Y., Shao, L., Li, J., Sun, C., Yu, K., Li, N., Taheri, M.L., Wang, H., Wang, J., Nastasi, M., 2018b. Radiation damage in nanostructured materials. *Prog. Mater. Sci.* 96, 217–321.
- Zhang, X., Misra, A., Wang, H., Shen, T.D., Nastasi, M., Mitchell, T.E., Hirth, J.P., Hoagland, R.G., Embury, J.D., 2004. Enhanced hardening in Cu/330 stainless steel multilayers by nanoscale twinning. *Acta Mater.* 52, 995–1002.
- Zhang, Y., Zuo, T.T., Tang, Z., Gao, M.C., Dahmen, K.A., Liaw, P.K., Lu, Z.P., 2014b. Microstructures and properties of high-entropy alloys. *Prog. Mater. Sci.* 61, 1–93.
- Zhang, Z., Mao, M.M., Wang, J., Gludovatz, B., Zhang, Z., Mao, S.X., George, E.P., Yu, Q., Ritchie, R.O., 2015c. Nanoscale origins of the damage tolerance of the high-entropy alloy CrMnFeCoNi. *Nat. Commun.* 6, 10143.
- Zhao, Y.F., Zhang, J.Y., Wang, Y.Q., Wu, K., Liu, G., Sun, J., 2019. Unusual plastic deformation behavior of nanotwinned Cu/high entropy alloy FeCoCrNi nanolaminates. *Nano Lett.* 11, 11340–11350.
- Zhao, Y.Y., Chen, H.W., Lu, Z.P., Nieh, T.G., 2018. Thermal stability and coarsening of coherent particles in a precipitation-hardened (NiCoFeCr)94Ti2Al4 high-entropy alloy. *Acta Mater.* 147, 184–194.
- Zheng, S., Beyerlein, I.J., Carpenter, J.S., Kang, K., Wang, J., Han, W., Mara, N.A., 2013. High-strength and thermally stable bulk nanolayered composites due to twin-induced interfaces. *Nat. Commun.* 4, 1696.
- Zhou, H., Li, X., Qu, S., Yang, W., Gao, H., 2014. A jogged dislocation governed strengthening mechanism in nanotwinned metals. *Nano Lett.* 14, 5075–5080.
- Zhu, Y., Li, Z., Huang, M., Liu, Y., 2015. Strengthening mechanisms of the nanolayered polycrystalline metallic multilayers assisted by twins. *Int. J. Plast.* 72, 168–184.
- Zinkle, S.J., Was, G.S., 2013. Materials challenges in nuclear energy. *Acta Mater.* 61, 735–758.